

1 **Assessing the impact of automatically derived depth**
2 **phases on the determination of earthquake hypocentres**
3 **– application to the South America subduction zone**

4 **Alice Blackwell¹, Timothy Craig², Sebastian Rost¹, Thomas Garth³, and Ryan**
5 **Gallacher³**

6 ¹Institute for Geophysics and Tectonics, University of Leeds, Leeds, UK

7 ²COMET, Institute for Geophysics and Tectonics, University of Leeds, Leeds, UK

8 ³International Seismological Centre, Pipers Lane, Thatcham, Berkshire, RG19 4NS, UK

9 This is a non-peer reviewed preprint submitted to EarthArXiv. The paper manuscript
10 has been submitted to the Journal of Geophysical Research: Solid Earth for peer review.

11 **Key Points:**

- 12 • We generate high resolution earthquake catalogues by combining *ad-hoc* array de-
13 tected depth phases with the ISC Bulletin.
- 14 • By including *ad-hoc* array-derived depth phases, we reduce depth error in 88.8%
15 of earthquakes.
- 16 • Using the new catalogues, we investigate the Wadati-Benioff zone structure and
17 reinterpret two major ($M_w \geq 7.5$) regional earthquakes.

Corresponding author: Alice Blackwell, ee18ab@leeds.ac.uk

Abstract

Accurate earthquake hypocentres are fundamental to a wide range of geophysical studies, yet source depth remains poorly constrained in teleseismic earthquake catalogues. Near source surface reflections such as pP , sP , and sS (known as depth phases) provide critical information for resolving hypocentral depth, particularly for intermediate-depth earthquakes. The number of depth phases reported by global earthquake monitoring agencies has declined significantly in recent decades, potentially reducing the precision of resolved earthquake depths. To address this, we automatically detect P , pP , sP , S and sS phase arrivals using teleseismic *ad-hoc* arrays. We detect these phases for earthquakes in the South American Subduction Zone (SASZ) at depths of 40–350 km and between m_b 4.7 to 6.5. The identified phases are integrated with the phases reported to the ISC Bulletin, and used to relocate earthquakes with ISCloc. We assess the impact of incorporating automatically detected, *ad-hoc* array-derived depth phases on earthquake relocations across the SASZ, and find an improvement in depth resolution for 88.8% of earthquakes. Using this enhanced catalogue we investigate the structure of the Wadati-Benioff zone, focusing on two significant earthquakes: the 2005 M_w 7.7 Tarapacá and 2019 M_w 8.0 Peru events. Finally, we successfully apply our methodology to deep focus earthquakes (350–700 km), which further define the deepest portion of the seismogenic slab. Our results demonstrate the potential for automatically detected, *ad-hoc* array-derived depth phases to substantially improve the accuracy of teleseismic earthquake hypocentres, and offer further constraint upon slab geometry and seismogenic structure.

Plain Language Summary

Finding earthquake hypocentres is important for investigating and understanding the Earth’s interior, however earthquake depth is typically poorly constrained when local seismic networks are limited. By using depth phases (near-source surface reflections, such as pP) earthquake depth, and therefore the overall earthquake hypocentre, can be determined more accurately using distant seismic station data. In this paper, we create *ad-hoc* seismic arrays from available teleseismic stations, in order to detect small amplitude P and S coda depth phases automatically. We apply our approach to the entire South American Subduction Zone (SASZ), and use our *ad-hoc* array-derived phases alongside the reported phases in the International Seismological Centre Bulletin to relocate the earthquakes using ISCloc. Our new continental-scale catalogue of earthquakes, demonstrates an increased depth resolution for 88.8% of earthquakes. Using the catalogue, we assess the structure of the Wadati-Benioff zone and consider the impact of our results upon the interpretation of two major earthquakes: the 2005 M_w 7.7 Tarapacá and 2019 M_w 8.0 Peru events. Overall, we show that automated detection of depth phases using *ad-hoc* arrays can improve the accuracy of earthquake hypocentres, and the resulting catalogues can further constrain slab geometry and stress distribution.

1 Introduction

The accurate location of earthquakes using globally-distributed seismic data underpins a wide range of solid-Earth geophysics, from seismic hazards assessment to nuclear security, regional tectonics to global-scale tomographic imaging. The depth of an earthquake is generally the least well determined dimension of an earthquake hypocentre, particularly when locating an earthquake using teleseismic (i.e. seismic phases recorded 30–90° from the source) phases. This can be mitigated by using near-source surface reflections arriving at a station shortly after their related direct arrival (e.g. pP and sP in the coda of P , sS in the coda of S), known as depth phases. This is effective due to the relative delay times between a direct arrival and the depth phases, which provide crucial constraints on the source depth of an earthquake, and are largely independent of the lateral location or origin time.

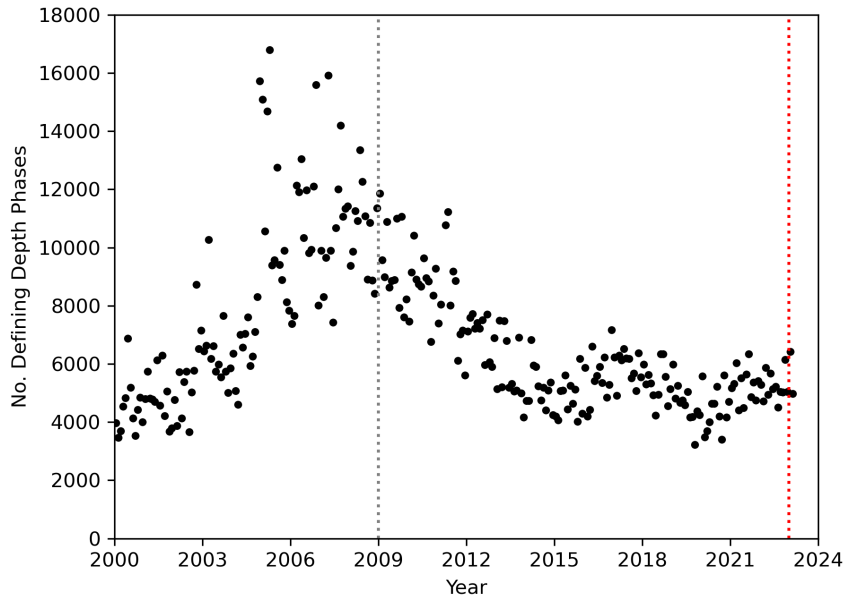


Figure 1. Number of depth phases (pP , sP , pwP , sS and surface reflected core phases) defining ISC earthquake hypocentres against the year the earthquake occurred (ISC, personal comms.). Grey dotted line highlights the beginning of 2009, where numbers begin to decline. Red dotted line shows the beginning of 2023, where the reviewed ISC catalogue approximately ends at time of writing.

68 Whilst the identification of distinct depth phases is difficult for earthquakes at shal-
 69 low depth due to overlap and interference with the direct phase, for earthquakes deeper
 70 than ~ 25 km the incorporation of a significant number of depth phases can result in high-
 71 precision depths and therefore improved hypocentre resolution. This is further comple-
 72 mented by the vast data coverage offered by routinely operating seismic stations around
 73 the world, which opens up the potential to expand high-precision earthquake relocation
 74 to unprecedented regions and scales. The increasing coverage of seismic data combined
 75 with the detection and application of depth phases can help to enhance our understand-
 76 ing of the intermediate-depth and deep focus seismicity, typically associated with sub-
 77 duction, and therefore the evolution of subducted slabs as they descend into the man-
 78 tle.

79 In the last 2 decades the number of depth phases reported from global seismic mon-
 80 itoring agencies to the International Seismological Centre (ISC), which is responsible for
 81 collecting and preparing the definitive summary of world seismicity, has substantially de-
 82 creased. This is likely due to the technical difficulty of picking depth phases coupled with
 83 limited picking resources at data centres. Consequently, the number of depth phases used
 84 in ISC relocations has dropped from ~ 8000 - $17,000$ to ~ 4000 - 7000 per month (Figure 1).
 85 Without the incorporation of depth phases, teleseismic hypocentres of relatively deep
 86 earthquakes (≥ 25 km) will have reduced depth resolution, leading to increased uncer-
 87 tainty in the other location parameters (lateral location and origin time). Therefore, there
 88 has been increased motivation to pick depth phases, either manually or automatically,
 89 to backfill the lack of reported depth phases and improve their earthquake relocations.

90 Blackwell et al. (2024) developed a new approach building on the work of Florez
 91 and Prieto (2017) to leverage the growing density of routinely-operating seismic stations,
 92 where the waveforms are openly accessible. This approach relies on assembling and pro-

93 cessing *ad-hoc* arrays to increase the signal-to-noise ratio of the phases (Ward et al., 2023),
 94 and automatically picking the beams derived from these *ad-hoc* arrays for P , pP and sP
 95 arrivals expressly to improve depth determination in Peru and northern Chile. The ap-
 96 proach of Blackwell et al. (2024) does not account for 3D variations in earthquake lo-
 97 cation and depth, nor does it incorporate depth phase bounce point corrections when
 98 determining earthquake depth. These are significant assumptions to apply to regions in
 99 South America, given the local Andean mountain range and associated crustal geome-
 100 tries (Craig, 2019), as is the assumption (common in teleseismic studies) that lateral lo-
 101 cation is unchanged when re-determining hypocentre depth. We can account for these
 102 assumptions by integrating the increased observational data available, using the approach
 103 outlined in Blackwell et al. (2024), with a more comprehensive location procedure, such
 104 as the ISC relocation algorithm, ISCloc (Bondár & Storchak, 2011). ISCloc calculates
 105 the earthquakes latitude, longitude, origin time and depth as well as determining the un-
 106 certainty in these parameters through an iterative linearized inversion. Travel times are
 107 calculated using the ak135 1D global velocity model (Kennett et al., 1995) and depth
 108 phase bounce point corrections are calculated from a 0.5 degree resolution topography
 109 (Engdahl et al., 1998; Bondár & Storchak, 2011).

110 In this paper, we test the impact of adding automatically derived depth phases to
 111 the wider set of seismic phases reported in the ISC Bulletin, using an expansive dataset
 112 encompassing the South American Subduction Zone (SASZ) and the ISCloc location al-
 113 gorithm. We show an improvement in the depth resolution of both the previous cata-
 114 logue reported by Blackwell et al. (2024) and the ISC Bulletin in the region, demonstrat-
 115 ing the benefits of augmenting a phase catalogue with *ad-hoc* array determined depth
 116 phases. Furthermore, we also investigate the impact of the newly relocated earthquakes
 117 upon the current understanding of the Wadati-Benioff zone (Wadati, 1935; Benioff, 1949)
 118 in northern Chile, the 2005 M_w 7.7 Tarapacá and 2019 M_w 8.0 Peruvian earthquakes.
 119 As part of this work, we extend the approach of Blackwell et al. (2024) to accommodate
 120 transverse-component *ad-hoc* array data for the detection of the direct S wave and its
 121 principal depth phase, sS , and further apply this method to relocate deeper earthquakes.

122 1.1 South American Subduction Zone (SASZ)

123 At the SASZ margin the Nazca and South American plates converge, as the Nazca
 124 plate subducts eastwards beneath South America. The margin extends from approxi-
 125 mately 6°S to 45°S in latitude, with the plates converging at ~ 5.6 –6 cm/yr in the di-
 126 rection of ~ 81 –83°N (Trenkamp et al., 2002). This encourages increasingly oblique con-
 127 vergence north of Chile, where the subduction trench curves westward (Rodríguez et al.,
 128 2024). The down-going Nazca plate in the SASZ has a number of bathymetric features
 129 (Figure 2) which are thought to influence seismicity and slab geometry in the region, such
 130 as fracture zones and ridges (Espurt et al., 2008; Bilek, 2010; Gao et al., 2021), and two
 131 named flat slab sections – the Peruvian and Pampean flat slabs (Flament et al., 2015).
 132 The margin also has associated arc volcanism; the locations of the Holocene volcanoes
 133 are illustrated in Figure 2. By extending the approach of Blackwell et al. (2024) to in-
 134 clude the entire SASZ, and incorporating new phases (S and sS), we aim to generate
 135 catalogues which can be used to assess further links between seismicity and the back-
 136 ground geodynamic setting. In the later stages of this work, we consider the implications
 137 of the revised seismicity catalogue on our understanding of the geometry and dynam-
 138 ics of the Wadati-Benioff zone and subducted plate, as well as for understanding the seis-
 139 mic activity in areas which hosted large-magnitude intraslab earthquakes (the 2005 Tara-
 140 pacá and 2019 northern Peru earthquakes).

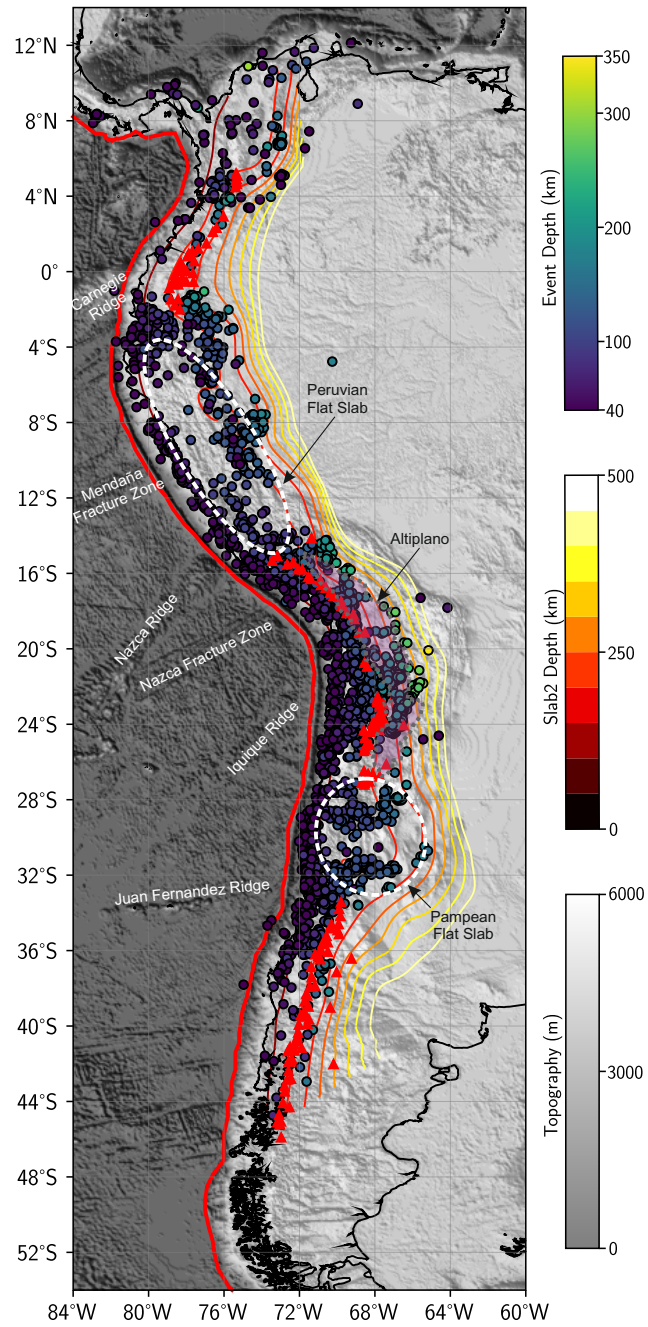


Figure 2. Map of the initial earthquake catalogue (circles) used for the SASZ intermediate-depth earthquake relocation. The thick red line shows the location of the subduction trench, and red triangles represent the locations of Holocene volcanoes (Global Volcanism Program, 2024). Other bathymetric and slab features are labelled (Zandt et al., 1994; Espurt et al., 2008; Bilek, 2010; Flament et al., 2015).

2 Earthquake relocation with ISCloc

We build upon and apply the methodology documented in Blackwell et al. (2024), to determine arrival times for teleseismic P , pP , sP , S and sS phases from array processed data. This aims to boost the signal-to-noise ratios of typically very small amplitude arrivals, relative to what is possible with a single seismic station. The arrays are assembled for each earthquake from the available teleseismic stations using unsupervised machine learning and are used for phase detection (further detail can be found in Section 2.3). We then combined these *ad-hoc* array determined arrivals with previously reported phase arrivals (archived at the ISC) and use the combined dataset to relocate earthquakes using ISCloc (Bondár & Storchak, 2011) (which solves for earthquake latitude, longitude, depth and origin time). We begin with an initial earthquake hypocentre catalogue for the SASZ – the selection of which is described in Section 2.1 – which we aim to refine by increasing the number of depth phases available for hypocentre determination. We will demonstrate the methodology with an example earthquake (m_b 6.0 from 25th July 2016, located in Chile) to illustrate the *ad-hoc* array processing and analysis steps.

2.1 Initial catalogue

The approach we have developed looks to refine intermediate-depth earthquake hypocentres which have already been determined by an external agency. For our initial SASZ earthquake catalogue, we take all earthquakes recorded in the ISC catalogue along the South American Subduction Zone from 01/01/1995 to 09/09/2024, with depths of 40–350 km. In keeping with the conclusions of Blackwell et al. (2024), we do not consider earthquakes shallower than 40 km, as the direct and depth phases are likely to overlap, and we limit the magnitudes for which we attempt relocation to m_b 4.7 – 6.5. The results of this search form the initial catalogue for our earthquake relocation approach, containing 2877 earthquakes (Figure 2).

2.2 Data processing

For each earthquake in the initial catalogue taken from the ISC (see Section 2.1), all available BH* or HH* channel teleseismic data (recorded between 30-90° epicentral distance), and their metadata, are downloaded from open access FDSN servers using ObspyDMT (Hosseini & Sigloch, 2017). These data are then pre-processed to prepare for the array-based approach discussed in Section 2.3.

We discard traces with gaps or missing data, and rotate horizontal components into the N and E orientations (if they are not already), using the component orientation stored in the metadata. The instrument responses are then deconvolved from the waveforms, and waveform data are converted to velocity, linearly detrended, demeaned, have a 5% end taper applied, bandpass filtered, are resampled to 10 Hz, and are normalised to their peak absolute amplitude. The bandpass filter applied depends on the component. Z-component data are filtered between 0.1-1.0 Hz, whilst horizontal component data are filtered between 0.03-0.2 Hz. For the duration of the seismic data processing, the Z components and horizontal components are handled independently, with horizontal components for a station only being processed if the station has 3-component data. Figure 3 summarises the data processing workflow.

2.3 Detecting P , pP , sP , S and sS picks using adaptive *ad-hoc* arrays

To determine the P , pP , sP , S and sS phases, used to refine the earthquake hypocentres (see Section 2.5), array processing is applied to boost the phase signal-to-noise ratios for automatic picking. A summary workflow of the array processing steps and phase identification is shown in Figure 4.

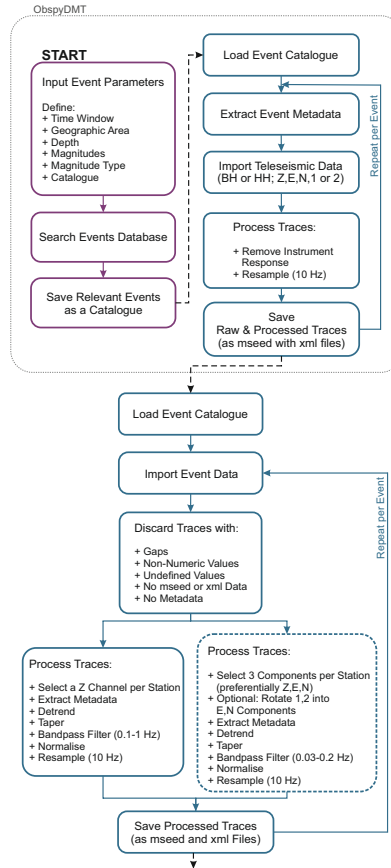


Figure 3. Summary workflow for processing 3-component teleseismic data for array processing in Section 2.3.

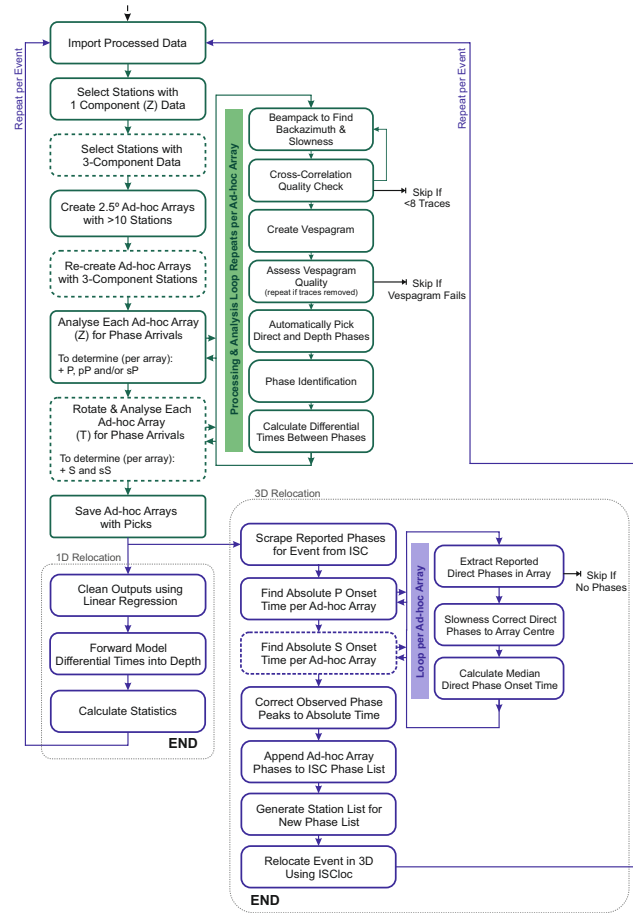


Figure 4. Summary workflow for relocating an earthquake using array processing described in Section 2.3, 2.4 and 2.5, including 1D relocation discussed in Blackwell et al. (2024). Dashed boxes indicate steps associated with S coda arrivals.

188

2.3.1 Creating ad-hoc arrays

189

190

191

192

193

194

195

196

197

198

199

200

For an earthquake with pre-processed Z component seismic data, stations are grouped into *ad-hoc* arrays using a combination of DBSCAN clustering (Ester et al., 1996) and Ball-Tree nearest neighbour algorithms (Pedregosa et al., 2011; Ward et al., 2023; Blackwell et al., 2024). The DBSCAN algorithm searches for sufficiently dense station distributions to form arrays with at least 10 stations within a 2.5° aperture, and identifies a central core station per array. The nearest neighbour algorithm selects the stations within the aperture of each core station to generate *ad-hoc* arrays. For the example earthquake, which occurred on 25th July 2016 in Chile at (26.1551°S , 70.4548°W), there are 1789 stations with processed Z-component data, which are clustered into 88 *ad-hoc* arrays containing 1229 of the available stations (Figure 5). Therefore, there are 560 stations with Z-component data which were not incorporated into an *ad-hoc* array – these stations are located too sparsely to generate an array which fits the density parameter.

201

202

203

204

205

206

207

208

209

210

211

212

213

To process *P* coda arrivals (hereby referring to *P*, *pP* and *sP*) the Z-component seismic data are arranged into *ad-hoc* arrays. For targeting *S* coda arrivals (hereby referring to *S* and *sS*, *S* coda processing is optional throughout this workflow), the available 3-component stations are assembled into the same *ad-hoc* arrays defined for *P* coda arrivals. Typically there are fewer stations available within an *ad-hoc* array which have data available for all 3 components, this can cause a number of 3-component *ad-hoc* arrays to have less than the required 10 stations or no stations at all. For the SASZ, 285,213 *ad-hoc* arrays are generated for the entire initial catalogue using Z component data, and only 89,024 *ad-hoc* arrays with 10 or more stations are re-created using 3-component data (31.2%). For the example earthquake from 25th July 2016, there are 88 *ad-hoc* arrays created from the Z component data, with only 72 from the 3-component data. Despite the reduction in *ad-hoc* array quantity, designing the *S* coda workflow to be dependent upon the *P* coda workflow significantly simplifies the approach.

214

2.3.2 Determining best-fit backazimuth and slowness

215

216

217

218

219

220

221

222

223

224

After the *ad-hoc* arrays have been established, the approach can take advantage of array processing to boost the signal-to-noise ratios of the small-amplitude depth phases (*pmP*, *pP*, *sP* and *sS*). For both the Z-only and 3-component versions of each *ad-hoc* array, the best fitting backazimuth and slowness for the *P* and *S* waves are found directly from the station data by beampacking the arrivals. The Z component *ad-hoc* array data are trimmed around the ak135 (Kennett et al., 1995) modelled *P* arrival, and beamformed with a range of test slownesses (± 0.04 s/km in intervals of 0.001 s/km) and backazimuths ($\pm 15^\circ$ in 1° intervals) centred on the expected values calculated using ray tracing (Crotwell et al., 1999). The backazimuth and slowness which construct the largest amplitude beam are selected as the best fitting beamforming values.

225

226

227

228

229

230

231

232

233

234

For a 3-component *ad-hoc* array, the best fitting backazimuth found from the Z component data is used to rotate the horizontal components into radial and transverse orientations. If the Z component *ad-hoc* array fails to provide a beampack determined backazimuth, the theoretical backazimuth based on the initial catalogue hypocentre is used instead. Given that the approach intends to pick *S* and *sS*, the transverse (T) component is taken forward for further analysis. The best fitting slowness and backazimuth are searched for using the same beampacking approach applied to the Z component data. However this time the T component data is trimmed to include the ak135 (Kennett et al., 1995) modelled *S* arrival, and the test ranges straddle the expected *S* wave slowness and backazimuth.

235

236

237

238

Figure 6 shows examples of the beampacking parameter search to extract the best fitting slowness and backazimuth values for both *P* and *S* waves (filled red circles on a and d), and their resultant beams (c and f), for the same *ad-hoc* array. A comparison to the expected values is additionally provided (hollow red circle on a and d), and the

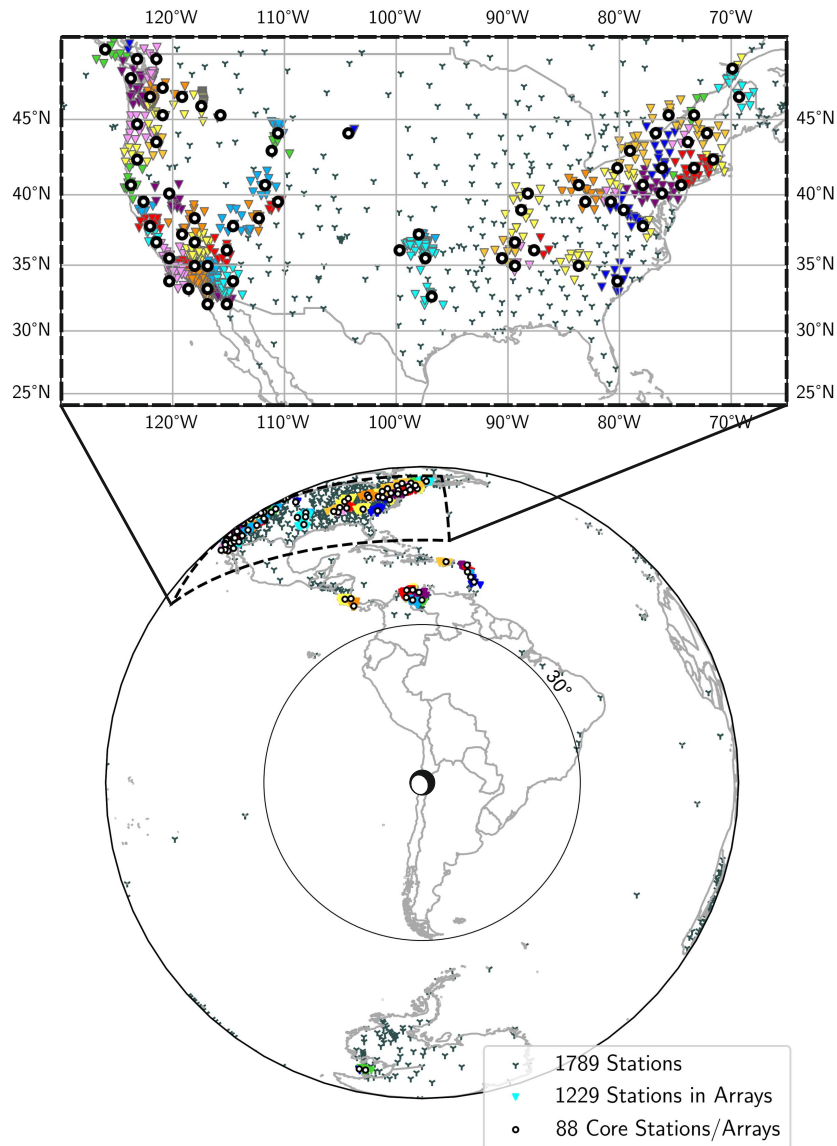


Figure 5. Example of the *ad-hoc* array creation process for a m_b 6.0 earthquake from 25th July 2016 located in Chile, showing a global distribution of teleseismic stations with processed Z components and the subsequent *ad-hoc* arrays (bottom), and a zoom in of the *ad-hoc* arrays created in the USA (top). The core stations per *ad-hoc* array are shown as thick black circles and the associated *ad-hoc* array stations as coloured triangles. The unused stations (grey Ys) are those removed via the DBSCAN routine, prior to the Ball-Tree process. The earthquake focal mechanism is taken from the Global Centroid Moment Tensor Project (GCMT) (Dziewonski et al., 1981; Ekström et al., 2012).

239 beams they construct (b and e). We find that using data-derived beamforming param-
 240 eters can significantly improve the wavelet geometry and signal-to-noise ratio of the depth
 241 phases since they account for near-receiver velocity structure variations, which acts to
 242 further suppress incoherent noise. This improves the ability to automatically pick the
 243 phases from the beams.

244 **2.3.3 Data quality control**

245 We apply two data quality tests to ensure that only *ad-hoc* arrays with clear, co-
 246 herent arrivals are considered for automatic picking. Our automatic picking routine (Sec-
 247 tion 2.3.4) relies upon fourth order phase weighted beams (Schimmel & Paulssen, 1997)
 248 for phase detection, we therefore also use phase weighted beams during our quality con-
 249 trol tests to ensure continuity between the two processes.

250 We first compare each trace in the *ad-hoc* array to the resultant optimum, phase
 251 weighted beam (created with the beampack determined slowness and backazimuth) us-
 252 ing cross-correlation. Any trace which has a cross-correlation coefficient less than 0.3 or
 253 which requires a timeshift greater than 0.5 seconds to align the trace to the beam, is dis-
 254 carded (Blackwell et al., 2024). If the *ad-hoc* array has less than 8 traces after this test,
 255 the *ad-hoc* array is removed from further analysis. If the *ad-hoc* array has 8 traces or more,
 256 the *ad-hoc* array analysis begins again, to re-determine the best fitting slowness and back-
 257 azimuth from the remaining traces, using the beampacking routine.

258 Second, we assess the coherency of the arrivals in the *ad-hoc* array data by con-
 259 sidering their slowness vespagram. Fourth order phase weighted vespagram beams are
 260 constructed using the same test slowness range used during the beampacking routine,
 261 and the beampack-determined backazimuth. On the resultant normalised vespagram, any
 262 peaks greater than 0.6 of the largest amplitude peak are selected, categorised into clus-
 263 ters using DBSCAN (Ester et al., 1996), and the cluster centres are extracted. These clus-
 264 ter centres are expected to represent the *P* or *S* coda arrivals for the *Z* and *T* compo-
 265 nent *ad-hoc* arrays, respectively, and therefore, are expected to align along the beampack-
 266 determined slowness. If the clusters are prominent at an unexpected slowness on the ves-
 267 pagram, that is an indication that the *ad-hoc* array is too complex or poor quality to au-
 268 tomatically pick. A set of criteria from Blackwell et al. (2024) are used to identify poor
 269 quality vespagrams. Specifically if the mean slowness is within 0.006 s/km of the expected
 270 beampack-determined slowness and the standard deviation of the cluster centres is <0.0105
 271 s/km, then the *ad-hoc* array passes the quality threshold. If these criteria are failed on
 272 either grounds, the *ad-hoc* array is discarded.

273 These quality control tests are separately applied to the *Z* and *T* component *ad-*
 274 *hoc* arrays for a given earthquake. However, for the *T* component *ad-hoc* array to be pro-
 275 cessed and analysed, the equivalent *Z* component *ad-hoc* array must have passed the qual-
 276 ity standards set. Furthermore, since the *T* component *ad-hoc* arrays are arranged sub-
 277 optimally to match those created with the *Z* component data, and often have a reduced
 278 number of traces per *ad-hoc* array (hence a 68.8% reduction in *ad-hoc* arrays with more
 279 than 10 stations), the *T* component *ad-hoc* arrays are more likely to be discarded by the
 280 quality control tests.

281 **2.3.4 Automatic phase detection and identification**

282 After the quality control routines have been applied, the *ad-hoc* array is eligible to
 283 be automatically picked using a threshold-based approach. We detect phases using the
 284 envelope of the normalised optimum, phase weighted beam. The dynamic threshold for
 285 a given *ad-hoc* array is determined from the distribution of amplitudes in the envelope
 286 by approximating the percentile (and thus, amplitude) after which larger amplitudes rep-
 287 resent significant signal (Figure 7). Peaks which exist above this dynamic threshold, and

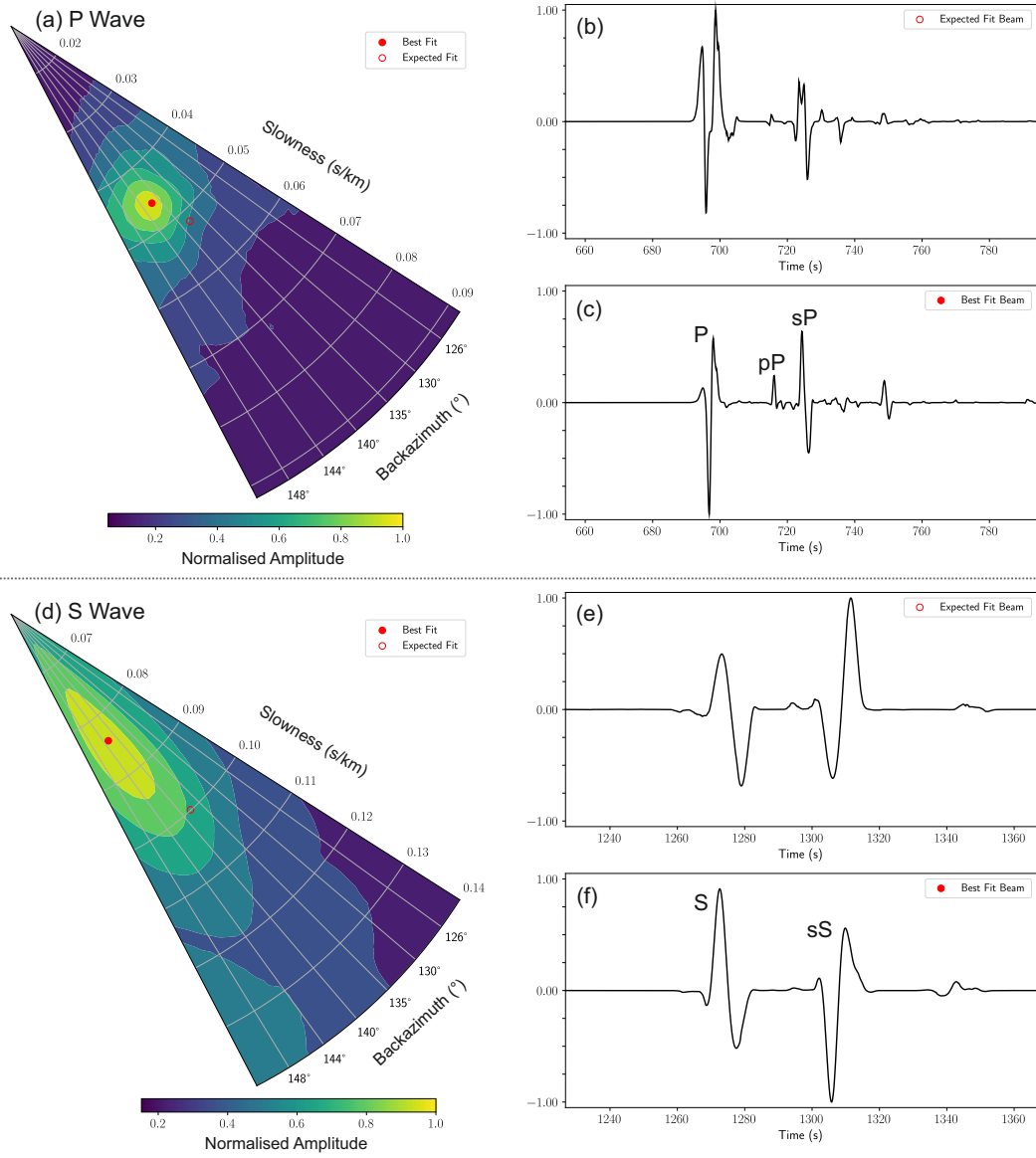


Figure 6. *P* and *S* wave amplitudes during beamforming in polar coordinates (backazimuth and slowness) to determine the best-fit backazimuth and slowness parameters directly from the *ad-hoc* array traces (a and d). The open red circle shows the expected slowness and backazimuth found through ray tracing and the corresponding phase-weighted beam in (b and e). The filled red circle shows the beampack derived values and the resultant phase-weighted beam in (c and f), showing the importance of using measured backazimuth and slowness values. Example from m_b 6.0 earthquake from 25th July 2016, *ad-hoc* array at 75.1° epicentral distance.

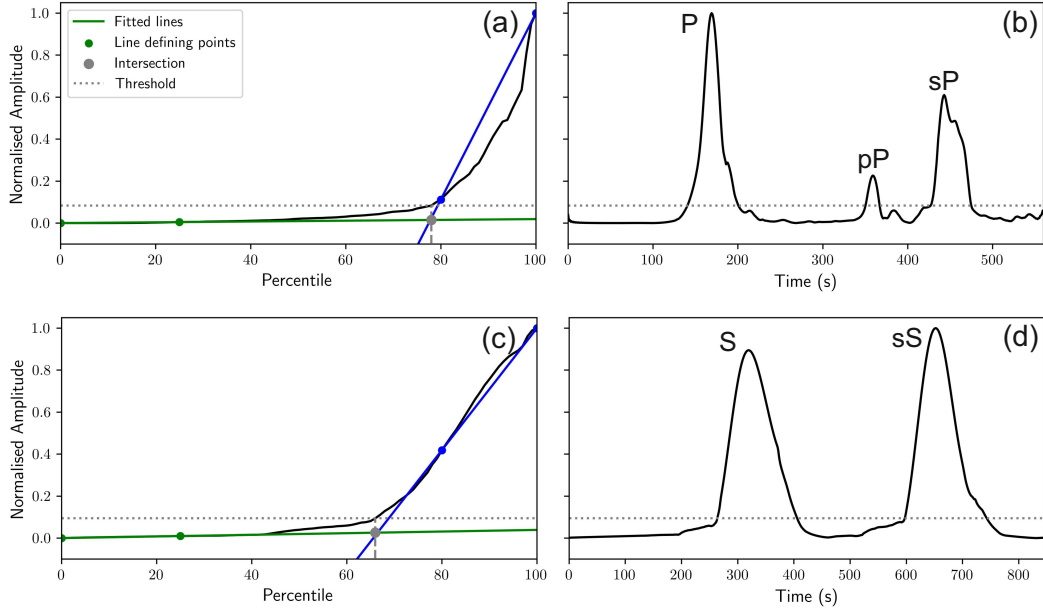


Figure 7. Example of the automatic picking threshold found for an *ad-hoc* array at an epicentral distance of 75.1° from the m_b 6.0 earthquake on 25th July 2016. Distribution of amplitude values for the *ad-hoc* array beam with respect to the percentile, the approximation of the beam with two lines, their intersection and the final threshold found for the Z (a) and T (c) components. Threshold relative to the envelope of the phase-weighted beam for the Z (b) and T (d) components.

288 have a prominence greater than 0.15 of the maximum peak found in the beam are selected as candidates for our phases. For phase detection the beam for the *ad-hoc* array is trimmed to only include the expected phases, using arrival times determined through the ak135 1D Earth model (Kennett et al., 1995) (e.g. 98% of the modelled P arrival time to 102% of the modelled sP arrival, for picking the P coda).

293 These candidates are subsequently passed to a phase detection routine to determine the most likely trio of peaks for P , pP and sP from the Z component data, and the most likely pair of peaks for S and sS from the T component data, when compared to the ak135 (Kennett et al., 1995) modelled arrivals. The best fitting sets of P and S coda peaks are selected as the final phase picks (note that P and S candidate peaks are independently assessed, Figure 8), however if multiple trios or pairs of phases are appropriate for the phases, the largest combined amplitude sets are selected. Equally if a suitable trio of P , pP and sP picks is not found, pairs of P and pP or P and sP are searched for instead. If there are no pairs found from the Z or T component data candidate picks, no phases are detected.

303 Each *ad-hoc* array for a given earthquake is analysed as described in this section (Section 2.3), with each Z component *ad-hoc* array processed and analysed before the equivalent T component data. Figure 9 illustrates the success rate for the 25th July 2016 earthquake, by showing which *ad-hoc* arrays produced phase picks for both the Z and T component data. The Z component data generated 88 *ad-hoc* arrays, resulting in 73 picked *ad-hoc* arrays (this could be P and either pP or sP , or all 3 phases). Whilst the T component data provided 72 *ad-hoc* arrays, using the previously defined Z component *ad-hoc* arrays, and 57 of those provided picks (both S and sS). The T component work-

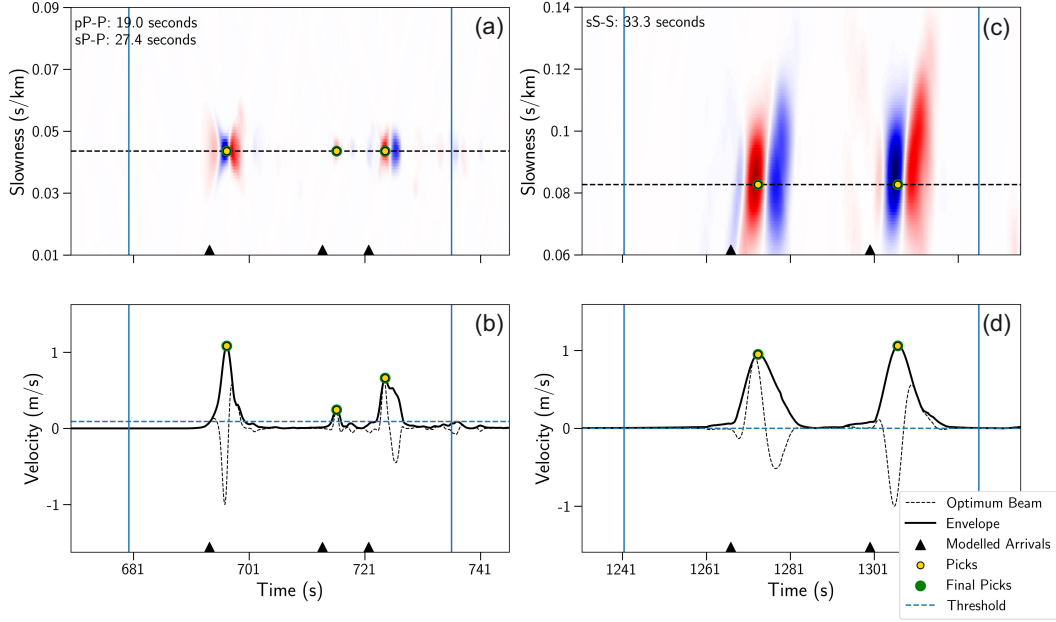


Figure 8. Example Z and T component *ad-hoc* arrays located 75.1° from the earthquake, their automatic picks and differential times between phases for the m_b 6.0 earthquake which occurred on 25th July 2016 in Chile. (a) and (b) are the vespagram and optimum beam respectively for the Z component *ad-hoc* array, whilst (c) and (d) are the vespagram and beam for the T component *ad-hoc* array. Blue vertical lines indicate the time window of data used for automatic picking.

311 flow suffers from a greater loss of data, due to the current requirement to construct the
 312 same *ad-hoc* arrays used for the Z component data, and link their processing to the suc-
 313 cess of the equivalent Z component *ad-hoc* array.

314 2.4 Converting amplitude picks to onset times

315 Previously Blackwell et al. (2024) used the relative timing of *P* wave coda arrivals
 316 determined from the *ad-hoc* arrays to directly determine earthquake depth. The pick-
 317 ing approach employed is designed to select the amplitude maxima of the phases, as op-
 318 posed to the phase onsets. This improves the ability to automatically and consistently
 319 pick phases, and proved sufficient for using the relative arrival times of the phases to de-
 320 termine earthquake depth. However, integrating the *ad-hoc* array-observed phases with
 321 phases reported by the ISC Bulletin, in preparation for relocation with ISCloc, requires
 322 us to correct the amplitude picks to onset arrival times.

323 For simplicity, we use *P* wave arrivals reported to the ISC to inform our required
 324 time-shift. We therefore developed an approach to extract the stations with time-defining
 325 (hypocentre defining) *P* phases reported for a given earthquake from the ISC Bulletin.
 326 We associate the stations with the *ad-hoc* arrays, slowness correct the phases to the ge-
 327 ometric centre of the *ad-hoc* arrays and calculate the median *P* onset time (when there
 328 are multiple) for a given *ad-hoc* array. The difference between the ISC catalogue derived
 329 *P* arrival time and the *P* amplitude pick from the *ad-hoc* array data is determined and
 330 used as the time-shift correction for the *pP* and *sP* phases. The ISC catalogue derived
 331 *P* arrival is used as the corrected *P* onset time.

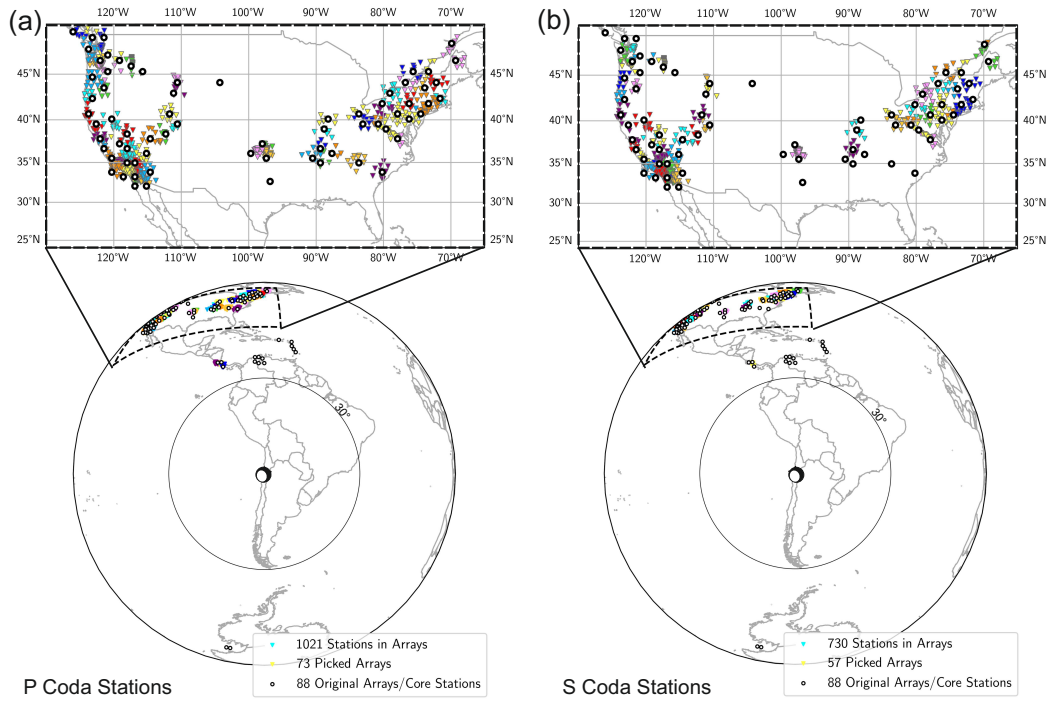


Figure 9. Global distribution of teleseismic stations in picked Z (*P* coda, a) and T (*S* coda, b) component *ad-hoc* arrays (bottom), and a zoom in of the USA *ad-hoc* arrays (top), from the m_b 6.0 25th July 2016 earthquake. The initially created core stations per *ad-hoc* array are shown as thick black circles and the stations of picked *ad-hoc* arrays as coloured triangles. The earthquake focal mechanism is taken from the Global Centroid Moment Tensor Project (GCMT) (Dziewonski et al., 1981; Ekström et al., 2012).

332 The manner of the approach means that if there is not a P arrival reported by a
 333 station within an *ad-hoc* array, that *ad-hoc* array's picks cannot be corrected and thus
 334 used. This is a common occurrence for earthquakes after 2022 at time of writing, as the
 335 ISC review process runs about 23-24 months behind real time. We therefore choose to
 336 only include earthquakes from 1995-2022 to achieve a stable dataset and the best pos-
 337 sible results. Our tests on the previously relocated intermediate-depth earthquake cat-
 338 alogues derived for Peru and northern Chile (Blackwell et al., 2024), when removing earth-
 339 quakes from >2022 , indicate that 25.5% (8815 out of 34598) of all *ad-hoc* arrays fail due
 340 to a lack of reported P arrivals. This converts into a loss of 11.6% earthquakes, where
 341 there are no P arrivals within the aperture of any of the *ad-hoc* arrays reported in the
 342 ISC catalogue, with a mean magnitude of m_b 4.99. We feel that the failure rates are man-
 343 ageable given the large initial dataset, and note that our catalogue will likely have a higher
 344 magnitude of completeness than originally intended.

345 We extend this methodology to the S wave coda picks, using exactly the same ap-
 346 proach, except ISC reported S arrivals are slowness corrected and used to convert the
 347 amplitude-based S and sS picks to onset times. Both corrections are limited by the avail-
 348 ability of direct P and S arrivals within a given *ad-hoc* array aperture, with S coda ar-
 349 rivals rarely being converted as a result. The example earthquake from the 25th July 2016
 350 only had 28.7% of *ad-hoc* arrays with S coda picks fail to be converted. However, 92.5%
 351 of all candidate T component *ad-hoc* arrays with picks for the SASZ fail as they have
 352 too few reported direct S wave arrivals, resulting in 80.0% of earthquakes with S coda
 353 picks without a single converted phase. For comparison, only 25.0% of Z component *ad-*
 354 *hoc* arrays with picks fail to be converted to absolute time, which translates to 22.2%
 355 of earthquakes. This illuminates an emerging issue with the low numbers of S waves re-
 356 ported by global seismic monitoring agencies.

357 We find a modal average delta of 0.87 seconds between the ISC derived P arrival
 358 and the *ad-hoc* array derived P amplitude pick, using the *ad-hoc* arrays from the Peru-
 359 vian and north Chilean relocated catalogues from Blackwell et al. (2024) (Figure S1 (d)).
 360 To utilize the *ad-hoc* arrays without a recorded P arrival, it might be possible to use the
 361 mode to correct the *ad-hoc* array phases to onset times. Alternatively there is the pos-
 362 sibility to use a machine learning picker to backfill *ad-hoc* arrays missing a recorded P
 363 onset. For this paper, we limit our onset correction to the use of the manually reviewed
 364 ISC catalogue P phases to ensure high quality results.

365 2.5 Set up and application of ISCloc

366 The online ISC Bulletin is dynamic, with the possibility of having new phases re-
 367 ported and added for a given earthquake after an ISC hypocentre is determined. In order
 368 to appropriately quantify the impact that adding *ad-hoc* array derived depth phases
 369 has on earthquake hypocentres, we run ISCloc twice, once with the phases currently re-
 370 ported for an earthquake in the ISC Bulletin, and once with the ISC reported phases plus
 371 the onset corrected *ad-hoc* array picks for P , pP , sP , S and sS , to ensure a fair compar-
 372 ison between the relocation outputs. We exclude ISC reported phases which are observed
 373 over 120° away from the ISCloc inputs to avoid complications with core depth phases,
 374 and we apply a linear inversion approach which seeds on the published ISC hypocentre.
 375 In line with Bondár and Storchak (2011), we require a minimum of 5 depth phases to
 376 secure depth resolution, and the ability to search/iterate without a fixed initial depth.
 377 This criterion is important since the addition of *ad-hoc* array phases could make the dif-
 378 ference between an earthquake being located with a fixed, grid defined depth or not, or
 379 even from having a robust hypocentre determined at all.

3 Catalogue analysis and interpretation

3.1 Assessing the impact of automatically derived depth phases

In this section we will compare the results from ISCloc when inputting the phases reported in the ISC Bulletin, versus the same input plus the *ad-hoc* array determined onsets for P , pP , sP , S and sS , for each earthquake. Henceforth, we refer to the online ISC Bulletin phases as the reported ISC inputs, and the ISC reported phases with the *ad-hoc* array phases will be referred to as the Augmented ISC inputs. The aim is to assess how the addition of automatically-derived depth phases affects both the hypocentre of a given earthquake and the error statistics.

1694 earthquakes have been augmented with 68,075 additional *ad-hoc* array derived phases, which provide a 50.0% increase in total depth phases used – 27.0% of these depth phases can be fitted within a small enough time residual to inform the earthquake hypocentre, referred to as time-defining, and are therefore used in the algorithm to increase depth resolution (Figure 10). The percentage of depth phases used to define the hypocentres is low suggesting that ISCloc acts as another quality control upon the depth phases, only allowing picks which agree with the determined epicenter to influence the inversion. Figures 10a and b also illustrate that the earthquakes with lower numbers of depth phases experience the greatest impact from the addition of *ad-hoc* array derived phases, as the numbers of (particularly time-defining) phases can increase by more than 100%, thus allowing greater depth resolution during the earthquake relocation. We will assess the value of the *ad-hoc* array phase additions in terms of hypocentre location and depth, the associated errors and the relation to earthquake magnitude in this section.

As a result of the incorporated *ad-hoc* array derived phases, there are 1057 earthquakes in the new SASZ intermediate-depth earthquake catalogue with free hypocentre solutions. For the earthquakes which were not relocated, most (784) fail to be relocated due to a lack of P and S picks reported in the ISC Bulletin, which are required to convert the amplitude picks to onset times. This is especially true for 2023/2024 earthquakes which are not currently considered for conversion (255 earthquakes with picks). An alternative independent method of reporting direct arrivals is needed to improve this in the future, potentially making use of machine learning seismic picking techniques (Münchmeyer et al., 2024). 79 earthquakes also have had their number of depth phases increased to more than 5, which allows ISCloc to solve for depth (assuming 5 depth phases are time defining) when *ad-hoc* array determined phases are incorporated. The addition of *ad-hoc* determined phases has decreased the mean depth error by 0.47 km (see Figure 11) when compared to the reported ISC catalogue (relocated using ISCloc and the reported ISC phases, without any additional phases), with depth error reductions for 939 (88.8%) of the 1057 earthquakes.

Depth errors are also unchanged for 68 earthquakes (6.4%), increase for 15 earthquakes (1.4%) and are newly determined for 34 (3.2%) earthquakes which now have a resolved depth due to the incorporation of *ad-hoc* array determined depth phases (i.e. taking them over the threshold value of 5 defining depth phases). The earthquakes which have newly resolved depths have an average magnitude of m_b 5.1, average depth of 86.8 km, and their epicentres are distributed across the entire SASZ. The few earthquakes with increased error using the augmented ISC catalogue input are typically caused by the additional time-defining phases producing large time residual misfits to the final hypocentre. Given our depth errors can increase when an earthquake has new input phases, it could be suggested that the errors defined for earthquakes are overly conservative and need to be increased to align with our error observations in the future.

We additionally note that a reduction in depth error is strongly correlated with the percentage increase in time-defining depth phases, which is largely a function of earthquake magnitude, and not necessarily related to an absolute number of additional phases

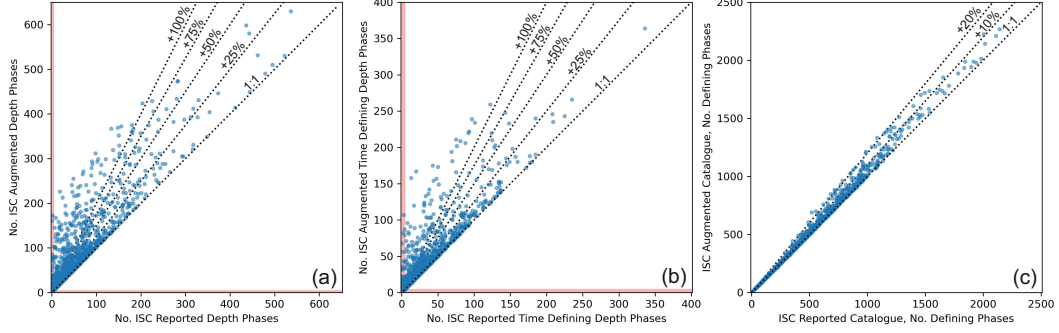


Figure 10. Number of input depth phases (a), time-defining depth phases (b) and all time-defining phases (c) for the ISC reported catalogue versus the augmented ISC catalogue. Red bands highlight earthquakes with less than 5 depth phases.

431 (Figure S2 (b) and (c)). Lower magnitude earthquakes are more likely to experience a
 432 greater percentage increase in time-defining depth phases, which translates to a greater
 433 reduction in depth error. Therefore augmenting the catalogue with *ad-hoc* array derived
 434 phases has a greater impact upon the relocations of earthquakes with low numbers of
 435 time-defining depth phases, which tend to be low magnitude earthquakes.

436 We also consider horizontal error reduction by calculating the area of the horizontal
 437 error ellipse, and notice that the addition of *ad-hoc* array phases minimally influences
 438 the horizontal error, with a mean reduction of 1.95 km². Despite this, some outliers exist
 439 where the horizontal error significantly decreased – notably there is an earthquake
 440 showing a reduction of 144 km². Further inspection of these examples shows that time-
 441 defining *sP* additions with small time residuals allow significant horizontal error reduction
 442 when few depth phases exist in the ISC reported catalogue, and the hypocentre was
 443 already poorly constrained; the example with the 144 km² reduction had an initial hori-
 444 zontal error area of >800 km². This suggests that improvement of horizontal and depth
 445 error is more sensitive to added *sP* than *pP* phases.

446 We test the sensitivity of depth error reduction to the addition of *pP* versus *sP* (see
 447 Figure S3). We see that a greater absolute number and proportion of *sP* phase additions
 448 to *pP* lowers the depth error for earthquakes by a mode of 0.14 and 0.71 km respectively.
 449 It is clear that a reduction in depth error benefits from a larger number of *sP* phases,
 450 likely due to the low numbers in the reported ISC catalogue compared to the number
 451 of reported *pP* phases.

452 3.2 Continental-scale application - South American Subduction Zone

453 The previous section has shown that a proportional increase in *P*, *pP*, *sP*, *S* and
 454 *sS* phases – determined through *ad-hoc* arrays – decreases the number of earthquakes
 455 where depth is defined from a pre-determined grid (fixed), decreases depth error in 88.8%
 456 of earthquakes and that *sP* phase additions influence the reduction in depth error to a
 457 greater extent than *pP*. Whilst the reductions are typically small (mean reduction of 0.47
 458 km), slight improvements in depth resolution across an earthquake catalogue can allow
 459 updates in the interpretation of a seismogenic region.

460 Figure 12 shows the new intermediate-depth earthquake catalogue for the SASZ,
 461 determined with the augmented ISC phase catalogues and ISCloc, with example cross
 462 sections highlighted (see supplementary material for figures showing all of the example
 463 cross sections). Cross sections C-C', D-D' and I-I' (Figure 13) illustrate the differences

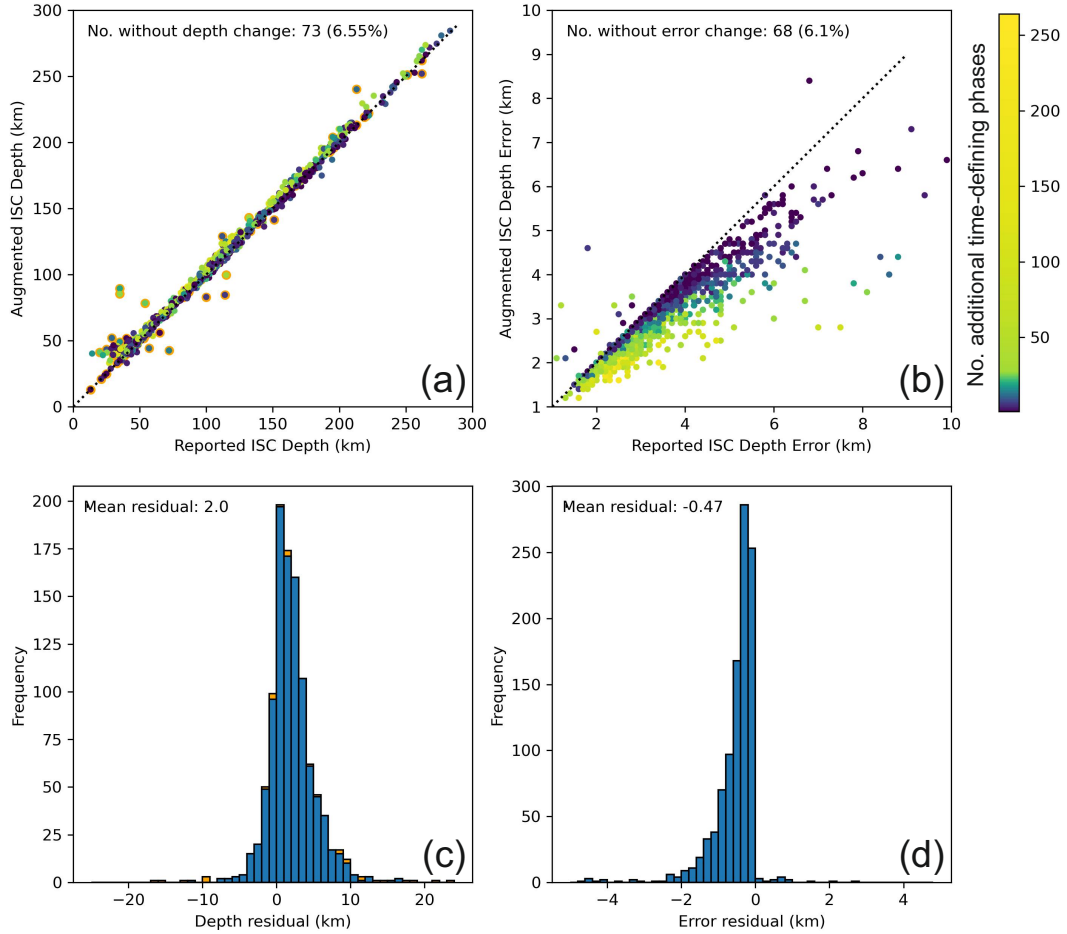


Figure 11. Comparison of depth and depth error between the reported ISC and augmented ISC inputs when applying ISCloc. (a) and (b) show the depth and depth error change when additional *ad-hoc* array phases are included. Both plots are coloured by number of additional time-defining phases, and (a) also has orange outlines for earthquakes which had fixed depths prior to the addition of phases. (c) and (d) are histograms showing the residual between the reported ISC and augmented ISC depths and depth errors respectively. (c) has orange bars indicating residual in depth when the fixed earthquakes are included. earthquakes which did not have new time-defining phases from the augmented ISC input are not plotted.

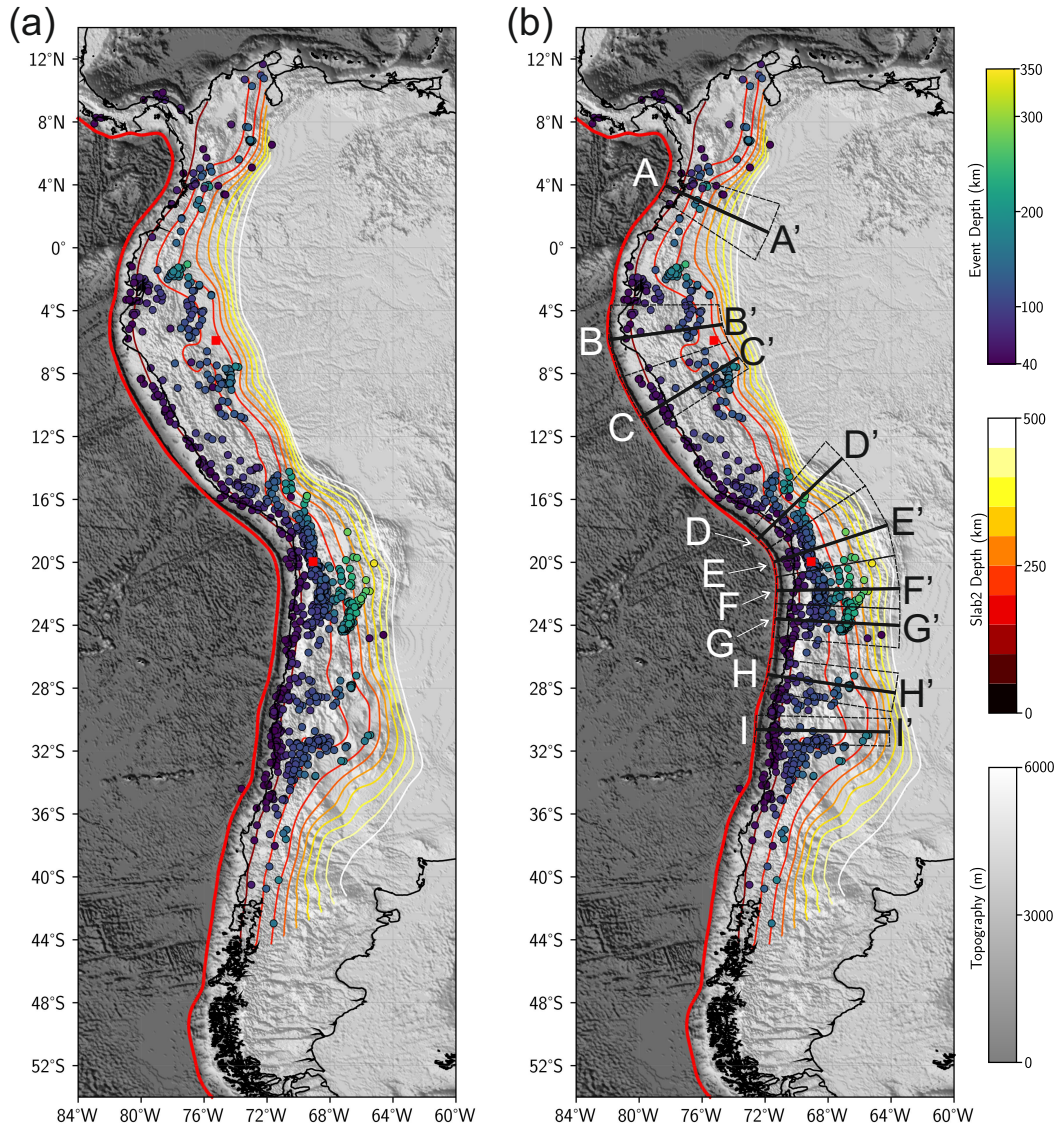


Figure 12. Map of the relocated intermediate-depth earthquakes (a), using the ISC augmented phase catalogues (which include *ad-hoc* array determined P , pP , sP , S and sS phases), with Slab2 contours (Hayes et al., 2018) and cross section locations (b). Red squares indicate the M_w 8.0 Peruvian earthquake and M_w 7.7 Tarapacá earthquake (Section 3.3).

464 between the earthquake hypocentres with and without the *ad-hoc* array determined phases,
 465 and when the phase catalogues are only augmented with the P coda picks. They also
 466 show previously identified features along the SASZ, including the Peruvian flat slab (Portner
 467 & Hayes, 2018) and Pucallpa nest (C-C') (Wagner & Okal, 2019; Sandiford et al., 2020),
 468 the transition from flat to normally dipping slab in northern Chile (D-D') (Ye et al., 2020),
 469 the geometry of the Pampean flat slab (Flament et al., 2015) and how the apparent seis-
 470 mogenic slab thickness can be decreased when the *ad-hoc* array derived phases are in-
 471 corporated into the earthquake relocation (I-I').

472 The cross sections shown in Figure 13 also demonstrate the limited effect includ-
 473 ing S and sS has on earthquake relocations. This is largely due to the relatively small

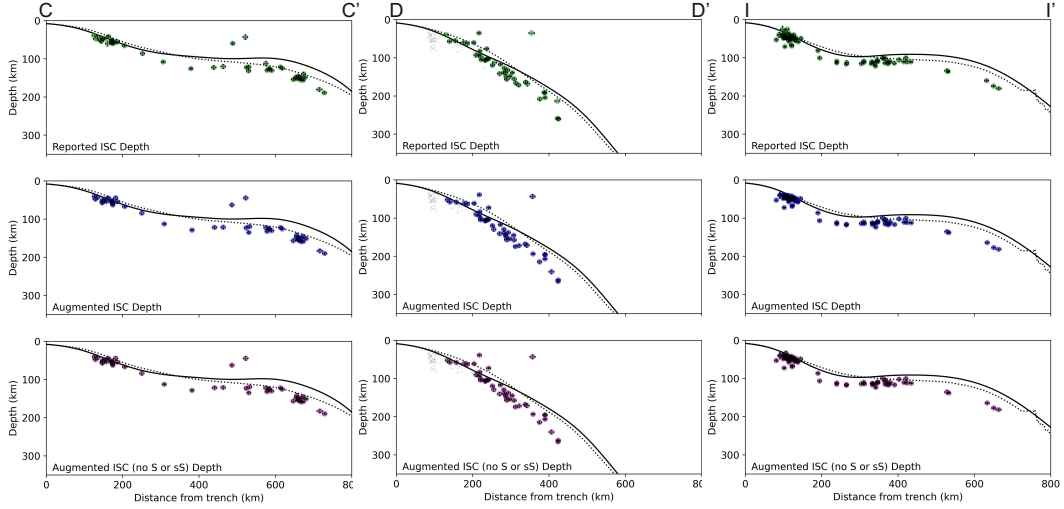


Figure 13. Example cross sections showing slab features, and differences between the earthquake catalogues determined using only the ISC reported phases (top), the ISC catalogue augmented with P and S coda picks (middle), and ISC catalogue augmented with only the P coda picks (bottom). Note that P coda picks refers to P , pP and sP , and S coda picks refers to S and sS . Horizontal and depth error bars are plotted per earthquake, and are often within the symbol diameter. Slab2 is plotted as a solid black line and Slab 1.0 is plotted as the dotted black line for comparison. Cross section locations shown in Figure 12.

474 number of S coda phases which were converted to absolute onset times, in order to use
 475 them with ISCloc. Only 830 sS phases were added to the reported ISC phase catalogues,
 476 compared to 20,196 pP and 20,442 sP phases (see Figure 10 to compare phase additions).
 477 However, 229 *ad-hoc* array derived sS phases became time-defining for the ISCloc hypocentre
 478 solutions, this forms 49.7% of the total time-defining sS phases and indicates that
 479 whilst the final sS phases numbers are currently small, they are enhancing the reported
 480 ISC catalogue, although, the inclusion of S and sS does not currently translate to large
 481 depth error reductions. To demonstrate this quantitatively, the augmented catalogue using
 482 both P and S coda arrivals, and the augmented catalogue using only the P coda phases
 483 have the same mean depth error reduction relative to the reported ISC catalogue (0.47
 484 km), and nearly the same mean residual (2.00 and 1.98 km, respectively) between the
 485 augmented and reported ISC earthquake depths when *ad-hoc* array determined phases
 486 are incorporated (see Figure 11 and S4).

487 We compare our new catalogue to the published ISC Bulletin and NEIC catalogues
 488 for the region in Figure 14. The selected cross sections indicate an aseismic gap at sub-
 489 duction depths of <90 km in the plate between two planes of seismicity, which further
 490 supports the presence of a DSZ in Chile. Section G-G' additionally displays an aseismic
 491 gap between approximately 380-420 km distance from the trench.

492 Although hypocentre differences between the published ISC catalogue and our cat-
 493 alogue are small (mean depth difference 0.51 km), improvements in depth error deter-
 494 mination can be seen clearly for two earthquakes closest to the trench on section E-E'
 495 and for the deepest earthquake on section G-G', where the published ISC catalogue has
 496 failed to determine a depth error due to insufficient depth resolution and our augmented
 497 catalogue has succeeded. However, the ISC published catalogue does demonstrate smaller
 498 depth errors by a mean of 0.3 km than our unsupervised ISCloc results (see Figure S12).
 499 This demonstrates the value of human seismic analysts during the relocation process.

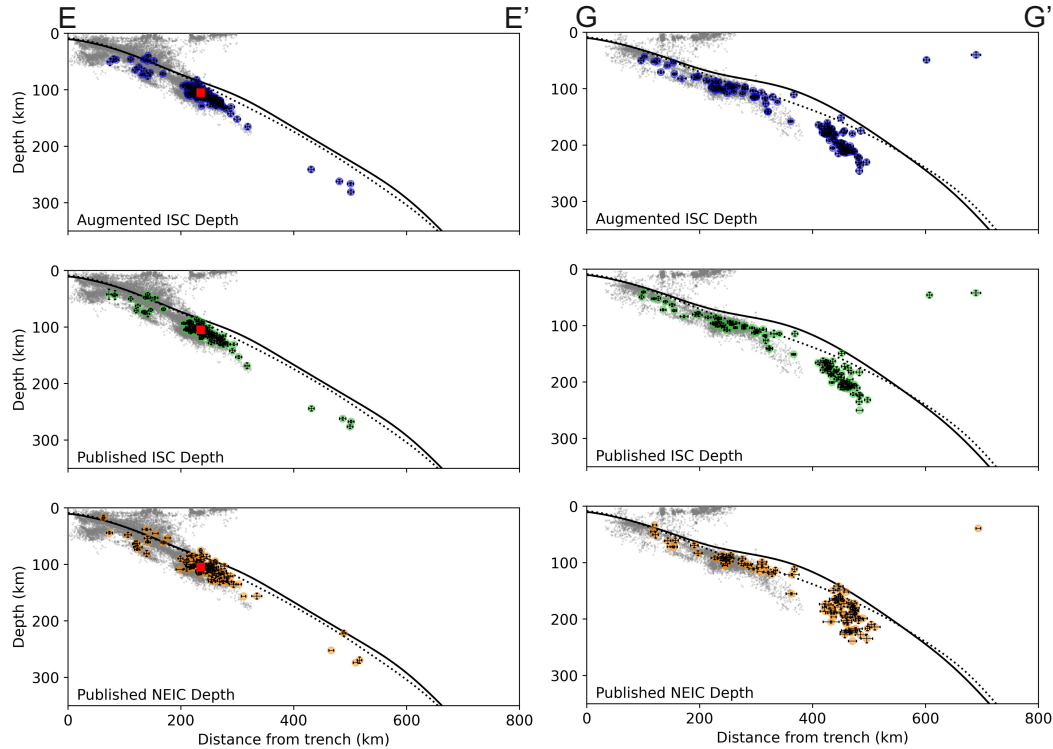


Figure 14. Example cross sections showing the difference between the augmented ISC catalogue from this study (top), published ISC earthquake catalogue (middle), and published NEIC catalogue (bottom). Horizontal and depth error bars are plotted per earthquake, they are often within the symbol diameter. Slab2 is plotted as a solid black line and Slab 1.0 is plotted as the dotted black line. cross section location shown in Figure 12. Red square shows location of M_w 7.7 Tarapacá earthquake (Section 3.3).

500 The NEIC catalogue generally demonstrates a larger scatter in seismicity, larger
 501 seismogenic thickness, and larger depth errors than both our and the published ISC cat-
 502 alogues, where independently determined earthquake depths are indicating more discrete,
 503 linear slab features. The mean depth difference between the NEIC published catalogue
 504 and our augmented ISC catalogue is 1.95 km (see Figure S13), and our catalogue reduces
 505 depth error by a mean of 0.93 km, whilst demonstrating a maximum reduction of 5 km.
 506 All example cross sections indicated on the map in Figure 12 can be seen in the supple-
 507 mentary material with both the ISCloc comparison and published catalogue compari-
 508 son versions.

509 It is also worth noting that published slab interfaces (Slab 1.0 and Slab2) seem to
 510 not fit the indicated slab behaviour from the new catalogue. For distances greater than
 511 400 km from the trench, both the Slab 1.0 (Hayes et al., 2012) and Slab2 models (Hayes
 512 et al., 2018) indicate that subducting slab thicknesses of up to 50 km exist between the
 513 slab interface and the intermediate-depth earthquakes (Figures 13 and 14). Given that
 514 oceanic crust thickness is typically approximated to be 7 km, and intra-slab earthquakes
 515 occur in the slab crust and/or upper mantle (Abers et al., 2013), a slab thickness greater
 516 than 20 km (Wang, 2002) above an intra-slab earthquake implies a poorly fitting slab
 517 interface model. The slab interface needs to be deepened with respect to distance from
 518 the slab to prevent interpretation of overly thick down-going slabs.

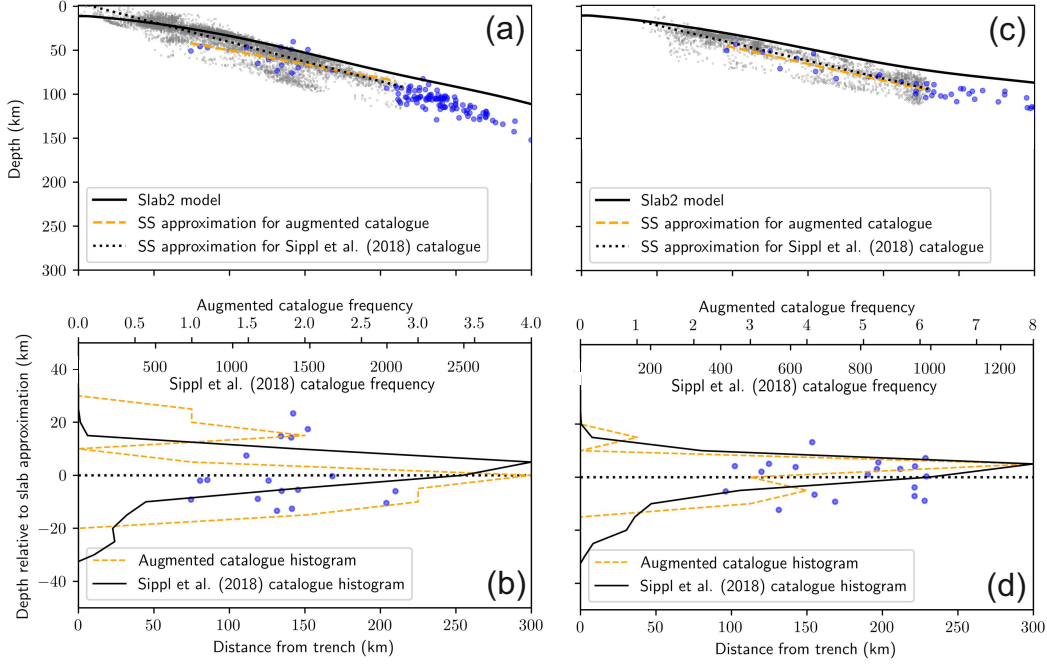


Figure 15. Zoomed-in E-E' (a) and G-G' (c) cross sections of the northern Chilean subducting slab, showing the augmented ISC catalogue (blue circles) and Sippl et al. (2018) catalogue (small grey circles) seismicity from the trench to 300 km inland, with seismogenic slab (SS) approximations for each catalogue. Slab 1.0 (Hayes et al., 2012) and Slab2 models (Hayes et al., 2018) shown in dotted and solid black, respectively. Histograms showing slab normal distributions of the augmented ISC and Sippl et al. (2018) catalogues for the E-E' (b) and G-G' (d) cross sections. Figure 12 shows the location of the sections on a map of the SASZ.

519

3.2.1 Structure of the Wadati-Benioff Zone in northern Chile

520

521

522

523

524

525

526

527

528

529

530

531

532

533

534

We use the resultant high resolution earthquake catalogue to investigate the structure of the Wadati-Benioff zone (Wadati, 1935; Benioff, 1949) in northern Chile, where a double seismogenic zone has been previously proposed by both Sippl et al. (2018) and Florez and Prieto (2019). Two Chilean cross sections (Figure 14) using the new earthquake catalogue qualitatively support the presence of a double seismic zone, when considered in tandem with local microseismicity data (Sippl et al., 2018). Using these cross sections, we interpret a broad convergence zone where the planes cannot be resolved, which ranges from approximately 100–160 km in depth. This corroborates the previously hypothesised 80–120 km deep convergence depth for this latitude of the Nazca subducting slab using microseismicity observations (Sippl et al., 2018, 2023), and the 142.1 km \pm 8 km convergence depth found using relatively relocated teleseismic data (Florez & Prieto, 2019) and ak135 (Kennett et al., 1995). Variation between our augmented catalogue depths and the Sippl et al. (2018) catalogue is expected since our dataset is derived using a different velocity model, and therefore will suffer a translational offset in depth relative to the microseismicity catalogue.

535

536

537

538

To quantitatively investigate the presence of a double seismogenic zone we follow the work of Brudzinski et al. (2007), who use slab normal hypocentre locations above the point of double seismogenic zone convergence to determine if a two-layer, bimodal distribution exists. Figure 15 (a) and (b) show sections E-E' and G-G' with both the aug-

539 mented catalogue earthquake hypocentres and the local Sippl microseismicity catalogue
 540 (Sippl et al., 2018), and their lines of best fit. The lines of best fit are subsequently used
 541 to correct the earthquake depths relative to the seismogenic slab geometry, and find the
 542 slab normal distribution of the hypocentres – shown in (b) and (d). The Sippl et al. (2018)
 543 catalogue here is limited to earthquakes categorised as either lower plane, upper plane
 544 or plate interface classes, in order to avoid loss of resolution from earthquakes which are
 545 not thought to form the double seismogenic zone. We note that these earthquake cat-
 546 egories, on the cross sections we inspect, end at approximately 230 km from the trench
 547 where plane convergence is expected, we therefore also limit the augmented ISC cata-
 548 logue and calculate the linear lines of best fit only for earthquakes within 230 km of the
 549 trench.

550 From these, we demonstrate an incipient bimodal distribution in both cross sec-
 551 tions from the Sippl et al. (2018) dataset, with a 20-30 km seismogenic gap apparent,
 552 although the lower plane seismicity is underdeveloped relative to the upper plane for both.
 553 The augmented ISC catalogue shows a weaker bimodal distribution in Figure 15b, with
 554 a more strongly defined lower plane and an approximately 20 km seismogenic gap. Whereas
 555 section G-G' on Figure 15d lacks enough earthquakes to define a confident histogram,
 556 yet still hints at bimodal distribution when considered in conjunction with the Sippl et
 557 al. (2018) catalogue slab normal distributions, despite offsets in both sections due to the
 558 use of different velocity models.

559 Whilst individually the augmented, high resolution catalogue results are not con-
 560 clusive enough to determine a double seismogenic zone, we believe that their results cor-
 561 roborate the presence of two planes seen in the microseismic data. Our findings reflect
 562 the resolution of the global catalogue determined histograms in Brudzinski et al. (2007),
 563 where maximum frequencies of 15 or 16 earthquakes define the north east Japanese dou-
 564 ble seismic zone with an approximately 30 km aseismic gap. The confidence in the global
 565 catalogue observed double seismic zones is increased when compared to the histogram
 566 resulting from the local catalogue (with maximum frequencies of 182 earthquakes), sim-
 567 ilarly to our comparison to the Sippl et al. (2018) catalogue histograms.

568 The Brudzinski et al. (2007) approach allows us to assess the likely presence of a
 569 double seismogenic zone, however to characterise the geometry and plane seismicity to
 570 a greater degree of accuracy using teleseismic datasets, the approach of Florez and Pri-
 571 eto (2019) could be reproduced. Their use of relative relocation, following the double dif-
 572 ference methodology, to define their earthquake catalogue allows the hypocentres to align
 573 along a coherent slab geometry. Thus enabling further analysis, such as investigating the
 574 controls upon the width of the aseismic gap and depth of double seismic plane conver-
 575 gence. For northern Chile, Florez and Prieto (2019) determine an $11.1\text{-}11.7 \pm 4$ km wide
 576 average aseismic gap, these values indicate that our slab-corrected augmented ISC cat-
 577 alogue and histogram driven results lack the precision to resolve a high accuracy mea-
 578 surement and likely mask a smaller aseismic gap. To continue research into the Chilean
 579 double seismogenic zone, we believe relative relocation of the earthquake hypocentres
 580 is necessary to enhance the prevalent slab geometries and ascertain higher degrees of ac-
 581 curacy.

582 **3.3 Comparison with finite-fault studies of major earthquakes**

583 A number of large magnitude earthquakes have occurred at intermediate-depths
 584 along the SASZ. From these two stand out – the M_w 8.0 Peruvian earthquake on 26th
 585 May 2019 and M_w 7.7 Tarapacá earthquake on 13th June 2005. Although both earth-
 586 quakes exceed the maximum magnitude at which we apply the approach developed in
 587 this paper, the rupture kinematics of these earthquakes have been studied in detail us-
 588 ing a combination of back-projection imaging, finite fault modelling and waveform in-

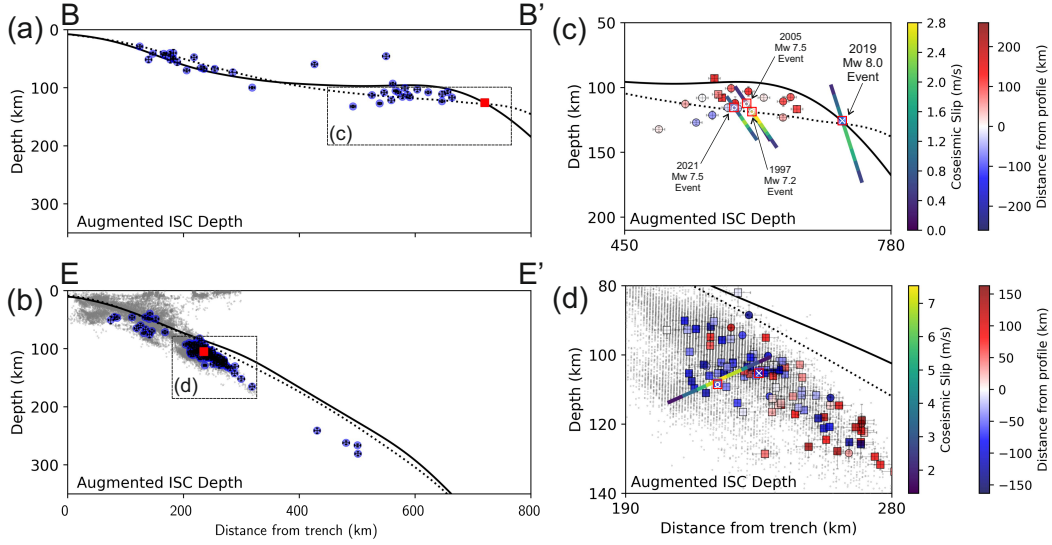


Figure 16. Example cross sections B-B' and E-E' showing the 2019 M_w 8.0 Peruvian earthquake (a) and 2005 M_w 7.7 Tarapacá earthquake (b) as red squares, alongside the augmented ISC catalogue (blue circles) and Sippl et al. (2018) catalogue (small grey circles) seismicity (only b/d). (c) and (d) show the earthquakes present in the zoomed-in boxes on (a) and (b), coloured by distance from the cross section and shown as circles if the earthquake pre-dates the major earthquake, or squares if it post-dates. Major earthquakes are marked by red-outlined squares, with the ISC hypocentres (International Seismological Centre, 2024) shown as white crosses and the USGS hypocentres (which are used for the finite fault models) indicated by white circles. Finite fault models from Zeng et al. (2025) are shown on (c) for earthquakes with $M_w \geq 7.5$, and the Hayes (2017) finite fault model is shown on (d) for the Tarapacá earthquake. All finite fault models display the maximum slip along the fault plane, projected onto the cross sections. Slab 1.0 (Hayes et al., 2012) and Slab2 models (Hayes et al., 2018) shown in dotted and solid black, respectively. Figure 12 shows the location of the sections on a map of the SASZ.

589 version (Peyrat et al., 2006; Delouis & Legrand, 2007; Kuge et al., 2010; Liu & Yao, 2020;
 590 Ye et al., 2020).

591 **3.3.1 M_w 7.7 Tarapacá earthquake**

592 The 2005 M_w 7.7 Tarapacá earthquake occurred in the upper double seismic zone
 593 of northern Chile. Finite-fault studies of this earthquake using combined seismic and geode-
 594 tic data conclusively show that it ruptured on a sub-horizontal, west-dipping plane, in
 595 an orientation consistent with the reactivation of faults from the outer rise (Peyrat et
 596 al., 2006; Delouis & Legrand, 2007). The earthquake was followed by a strong aftershock
 597 sequence (defined here as earthquakes post dating the mainshock). Many of the after-
 598 shocks have been relocated here using our new approach. Our improved hypocentres for
 599 moderate-magnitude seismicity delineate a clear sub-horizontal plane of seismicity in the
 600 source region of the Tarapacá earthquake, spanning roughly the same spatial extent as
 601 the down-dip width of the best available finite fault model from the USGS (Hayes, 2017).
 602 The USGS finite fault model is nucleated on the hypocentre from the NEIC PDE (white
 603 diagonal line, Figure 16), which is ~ 13.5 km further west than the ISC located hypocen-
 604 tre. Applying a similar shift to the entire finite fault model would result in a close match
 605 between the extent and orientation of the finite fault model and the aftershock cloud.

606 The aftershocks perhaps suggest a slightly shallower dip than used in the finite fault in-
 607 version. In this case, it is clear that the M_w 7.7 earthquake ruptured the full width of
 608 the upper seismic zone, which hosts the vast majority of seismicity with $m_b > 4.7$, and
 609 perhaps extended further into the aseismic region separating double seismic zones than
 610 is usually seen. However, it did not reach the lower seismic zone, which at these depths
 611 is only really apparent thanks to the dense microseismic networks available in northern
 612 Chile.

613 3.3.2 M_w 8.0 Peruvian earthquake

614 The 2019 M_w 8.0 intraslab earthquake beneath Peru has been well studied (e.g.,
 615 Hu et al., 2021; Vallée et al., 2023; Zeng et al., 2025). In Figure 16c, we show the finite
 616 fault models of Zeng et al. (2025) for comparison with our relocated moderate-magnitude
 617 seismicity, with the furthest east being the 2019 M_w 8.0 earthquake.

618 In contrast to the more productive aftershock sequence of the Tarapacá earthquake,
 619 the Peruvian earthquake had very few aftershocks, in keeping with most intermediate-
 620 depth earthquakes (e.g., Wimpenny et al., 2023), with no clear fault plane delineated.
 621 Luo et al. (2023) suggest that this earthquake ruptured through both seismic zones, as
 622 determined by Brudzinski et al. (2007). However, our relocations in this region remain
 623 insufficient to clearly distinguish a separation into two double seismic zones. Whilst we
 624 lack the resolution to separate the earthquake population into distinct seismic zones, the
 625 depth-extent of rupture (Zeng et al., 2025) is similar to the depth range over which we
 626 see moderate-magnitude seismicity distributed in our relocations.

627 The hypocentre location and mechanism of this earthquake (down-dip normal-faulting)
 628 suggest that it likely locates at, or near, the point of rebending at the downdip end of
 629 the Peruvian flat slab. However, it is more plausibly situated in the initial part of the
 630 bend – where the upper section of the plate is accumulating curvature – rather than the
 631 ‘unbending’ section, where the upper plane is instead in downdip compression (e.g., Craig
 632 et al., 2022; Sippl et al., 2022). Alongside the broad region of moderate-magnitude seis-
 633 micity slightly further up dip, this suggests that the termination of the Peruvian flat slab
 634 is likely to be slightly further east than currently incorporated in slab models (Hayes et
 635 al., 2018). Figure 16c also shows finite fault rupture models for other $M_w \geq 7.5$ earth-
 636 quakes in the Peruvian flat slab region, from Zeng et al. (2025). The rupture extent of
 637 these earthquake fits with the seismogenic width of the slab indicated by our relocated
 638 moderate-magnitude seismicity, indicating that our refined teleseismic hypocentres are
 639 now appropriately imaging the seismogenic structure of the slab, suitable of use in con-
 640 straining maximum magnitudes for seismic hazard.

641 4 Deep focus earthquakes

642 As described in Section 2, our approach is designed for the relocation of intermediate-
 643 depth earthquakes (Blackwell et al., 2024), and has been shown in Section 3 to increase
 644 the resolution of continental-scale earthquake catalogues. Given the relatively low num-
 645 bers of deep focus earthquakes in the SASZ, and their capacity to enhance the overall
 646 understanding of the region, we test the limits of our methodology and additionally re-
 647 locate these earthquakes.

648 Using the same time period and parameters in Section 2.1, except with a new search
 649 depth of 350-700 km, we find 48 candidate earthquakes in the ISC catalogue. 24 earth-
 650 quakes were successfully relocated, from the array processing stages through to the re-
 651 location using ISCloc, with 20 earthquakes failing to pass the *ad-hoc* array quality con-
 652 trol criteria or have detected phases, and 4 earthquakes failing during the step to timeshift
 653 the picked phases to absolute onset times. The addition of *ad-hoc* determined phases has
 654 decreased the mean depth error by 0.15 km (see Figure S14) when compared to the re-

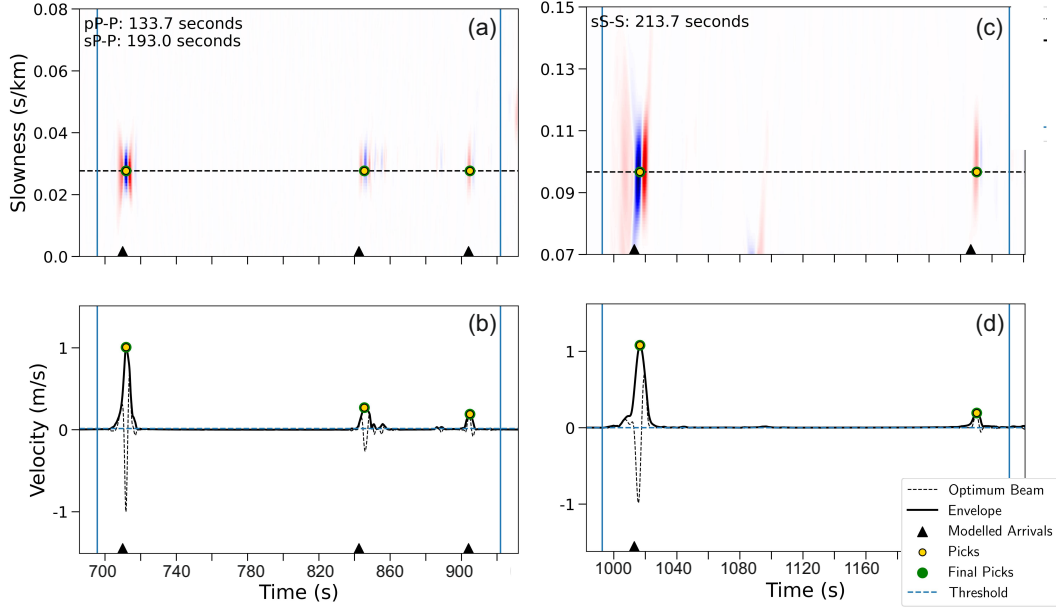


Figure 17. Example Z and T component *ad-hoc* arrays, their automatic picks and differential times between phases for the deep m_b 6.0 earthquake which occurred on 6th August 2022 in eastern Brazil. (a) and (b) are the vespagram and optimum beam respectively for the Z component *ad-hoc* array located 88.9° from the earthquake, whilst (c) and (d) are the vespagram and beam for the T component *ad-hoc* array located 61.5° from the earthquake. Blue vertical lines indicate the time window of data used for automatic picking.

ported ISC catalogue (relocated using ISCloc and the reported ISC phases, without any additional phases).

Figure 17 demonstrates the approach on an example m_b 6.0, deep (619.2 km according to the ISC) earthquake from 6th August 2022. 105 *ad-hoc* arrays with 1728 stations were created from a total of 2400 available teleseismic stations, resulting in 52 P , 52 pP , 17 sP , 1 S and 1 sS absolute onset picks. From inspection of this and other examples, we believe that the approach works well on deep focus earthquakes and therefore, we include them in our final relocated catalogue. Figure 18 demonstrates the relocated intermediate-depth and deep focus earthquake catalogues for the SASZ, with an example cross section. The cross section clearly shows the need for a deeper slab model with respect to distance from the subduction trench, and allows a more comprehensive understanding of slab geometry inland. Crucially, the ability to successfully use array processing on deep focus earthquakes, and detect small amplitude phases, opens up opportunity to expand our application of adaptive *ad-hoc* arrays to a broader range of earthquakes.

5 Conclusion

The ISCloc intermediate-depth earthquake relocations (solved for hypocentral latitude, longitude, depth and earthquake origin time) based upon the augmented ISC phase catalogue (ISC reported phases with additional automatically-derived P , pP , sP , S and sS arrivals) for the South American Subduction Zone show a decrease in depth error for 88.8% of earthquakes in our catalogue, and therefore a refinement in hypocentral depths. Significant improvements are particularly evident when comparing previous catalogue

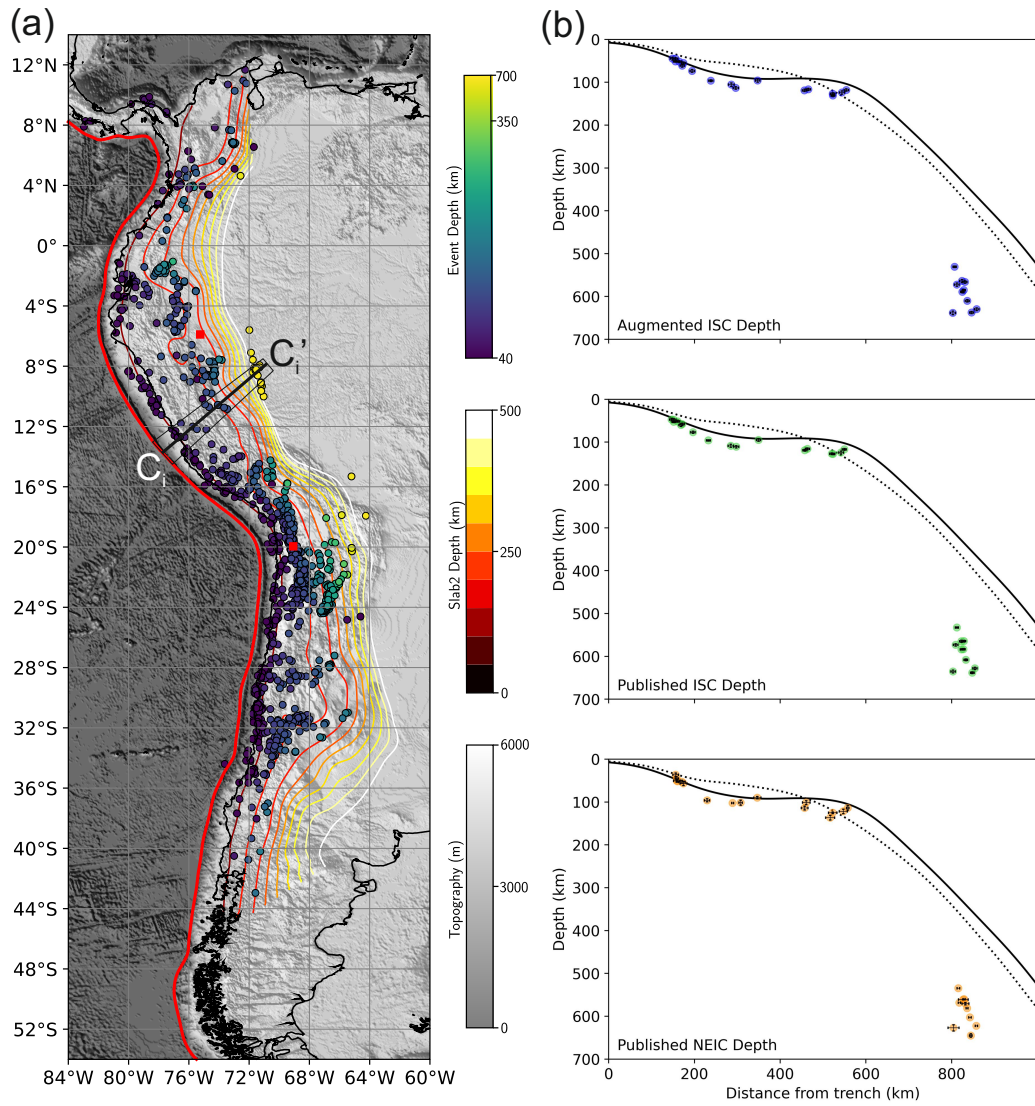


Figure 18. Map with Slab2 contours (Hayes et al., 2018) (a) and example cross section (b) of the final SASZ intermediate-depth and deep focus earthquake catalogues. (b) shows the difference between the augmented ISC catalogue from this study (top), published ISC earthquake catalogue (middle), and published NEIC catalogue (bottom). Horizontal and depth error bars are plotted per earthquake, they are often within the symbol diameter. Slab2 is plotted as a solid black line and Slab 1.0 is plotted as the dotted black line. Red squares show hypocentres of the M_w 7.7 Tarapacá earthquake and M_w 8.0 Peruvian earthquake (Section 3.3).

677 relocations based on *ad-hoc* arrays (Blackwell et al., 2024) to those enhanced by ISCloc,
 678 owing to its incorporation of bounce point and elevation corrections, and its simultane-
 679 ous inversion for hypocentre latitude, longitude, and depth. It is clear that automati-
 680 cally determined phase arrivals, from array processed teleseismic data, are a useful re-
 681 source to the wider community to improve earthquake locations and depths, and enhance
 682 interpretation. The greatest limitation of the presented approach is the conversion of the
 683 *ad-hoc* array determined amplitude picks to absolute phase onset times. We suggest an
 684 alternative method involving machine learning for this conversion, which could be used
 685 in future applications.

686 We use our new earthquake catalogue to investigate the Wadati-Benioff zone in north-
 687 ern Chile. We find that despite the improvements in depth resolution, our teleseismic
 688 earthquake catalogue cannot independently verify the presence of a double seismogenic
 689 zone in northern Chile, without reference to the local microseismicity catalogue created
 690 by Sippl et al. (2018). We additionally consider two major earthquakes from the South
 691 American Subduction Zone – M_w 7.7 Tarapacá earthquake and M_w 8.0 Peruvian earth-
 692 quake – and evaluate their aftershocks (which have been relocated by our approach) rel-
 693 ative to their finite fault models (Hayes, 2017; Zeng et al., 2025). Our high-resolution
 694 earthquake hypocentres reveal a well-defined sub-horizontal plane of seismicity in the source
 695 region of the Tarapacá earthquake, extending across approximately the same down-dip
 696 width as that of the USGS finite fault model (Hayes, 2017) yet at a shallower dip. In con-
 697 trast, our catalogue shows few aftershocks of the Peruvian earthquake and does not re-
 698 veal an associated plane. However, the finite fault model and its proximity to a broad
 699 region of seismicity up-dip suggests that the earthquake is a consequence of early slab
 700 rebending. This indicates that the distal bend of the Peruvian flat slab exists eastwards
 701 of existing slab models.

702 Finally, we test our approach by also relocating deep focus earthquakes associated
 703 with the SASZ, in order to comprehensively understand the geometry of the subduct-
 704 ing Nazca plate. These earthquakes demonstrate a mean depth error reduction of 0.15
 705 km, further validating the findings from the relocated intermediate-depth earthquake cat-
 706 alogue that *ad-hoc* array determined depth phases improve the depth resolution of tele-
 707 seismic earthquake catalogues.

708 Open Research Section

709 All seismic data used in this study are openly available from BGR at [http://eida](http://eida.bgr.de)
 710 [.bgr.de](http://eida.ethz.ch), ETH at <http://eida.ethz.ch>, GEONET at [http://service.geonet.org](http://service.geonet.org.nz)
 711 [.nz](http://service.geonet.org.nz), GFZ at <http://geofon.gfz-potsdam.de>, ICGC at <http://ws.icgc.cat>, INGV
 712 at <http://webservices.ingv.it>, IPGP at <http://ws.ipgp.fr>, IRIS at [http://service](http://service.iris.edu)
 713 [.iris.edu](http://service.iris.edu), KNMI at <http://rdsa.knmi.nl>, LMU at [http://erde.geophysik.uni-muenchen](http://erde.geophysik.uni-muenchen.de)
 714 [.de](http://erde.geophysik.uni-muenchen.de), NIEP at <http://eida-sc3.infp.ro>, NOA at <http://eida.gein.noa.gr>, ORFEUS
 715 at <http://www.orfeus-eu.org>, RESIF at <http://ws.resif.fr>, SCEDC at [http://](http://service.scedc.caltech.edu)
 716 service.scedc.caltech.edu, TEXNET at <http://rtserve.beg.utexas.edu>, UIB-
 717 NORSAR at <http://eida.geo.uib.no>, and USP at <http://sismo.iag.usp.br>. A full
 718 list of seismic networks used, and their DOIs, is provided in supplementary material. Fi-
 719 nal earthquake catalogues for the South American Subduction Zone are provided in sup-
 720 plementary material. The code is available at [https://github.com/AliceBlackwell/](https://github.com/AliceBlackwell/Depth.Phase.Array.Analysis)
 721 [Depth.Phase.Array.Analysis](https://github.com/AliceBlackwell/Depth.Phase.Array.Analysis).

722 Acknowledgments

723 AB was supported by the Leeds-York-Hull Natural Environment Research Coun-
 724 cil (NERC) Doctoral Training Partnership (DTP) Panorama under grant NE/S007458/1.
 725 TJC was supported in this work by the Royal Society under URF\R1\180088, URF\R\231019

726 and RF\ERE\210041, and also through COMET, which is the NERC Centre for the Ob-
 727 servation and Modelling of Earthquakes, Volcanoes and Tectonics, a partnership between
 728 UK Universities and the British Geological Survey. AB, TJC and SR were also partly
 729 supported by the Leverhulme Trust through Research Grant RPG-2021-336. Much of
 730 this work was undertaken on ARC4, part of the High Performance Computing facilities
 731 at the University of Leeds, UK, and using the ObsPy seismology toolbox for Python (Beyreuther
 732 et al., 2010).

733 The ISC (TG and RG) is supported by 80 Member-Institutions in 50 countries ([www](http://www.isc.ac.uk/members/)
 734 [.isc.ac.uk/members/](http://www.isc.ac.uk/members/) last access: June 2025), including the National Science Founda-
 735 tion award EAR 2414178 and the Royal Society award INT004. The ISC is also grate-
 736 ful to the following organizations that help to fund the ISC development projects: CTBTO,
 737 FM Global, the Lighthill Risk Network, AXA XL, USGS, SARA, GeoSIG, GaiaCode and
 738 MS&AD.

739 References

- 740 Abers, G., Nakajima, J., van Keken, P., Kita, S., & Hacker, B. (2013). Thermal-
 741 petrological controls on the location of earthquakes within subducting
 742 plates. *Earth and Planetary Science Letters*, *369-370*, 178–187. Re-
 743 trieved from <http://dx.doi.org/10.1016/j.epsl.2013.03.022> doi:
 744 10.1016/j.epsl.2013.03.022
- 745 Benioff, H. (1949). Seismic evidence for the fault origin of oceanic deeps.
 746 *Bulletin of the Geological Society of America*, *60*(12), 1837–1856. doi:
 747 10.1130/0016-7606(1949)60[1837:seftfo]2.0.co;2
- 748 Beyreuther, M., Barsch, R., Krischer, L., Megies, T., Behr, Y., & Wassermann,
 749 J. (2010, 5). ObsPy: A python toolbox for seismology. *Seismological Re-*
 750 *search Letters*, *81*(3), 530–533. Retrieved from <http://webdc.eu> doi:
 751 10.1785/gssrl.81.3.530
- 752 Bilek, S. (2010). Invited review paper: Seismicity along the South American subduc-
 753 tion zone: Review of large earthquakes, tsunamis, and subduction zone com-
 754 plexity. *Tectonophysics*, *495*(1-2), 2–14. Retrieved from [http://dx.doi.org/](http://dx.doi.org/10.1016/j.tecto.2009.02.037)
 755 [10.1016/j.tecto.2009.02.037](http://dx.doi.org/10.1016/j.tecto.2009.02.037) doi: 10.1016/j.tecto.2009.02.037
- 756 Blackwell, A., Craig, T., & Rost, S. (2024, 9). Automatic relocation of intermediate-
 757 depth earthquakes using adaptive teleseismic arrays. *Geophysical Journal In-*
 758 *ternational*, *239*(2), 821–840. Retrieved from [http://academic.oup.com/gji/](http://academic.oup.com/gji/article/201/3/1977/782891/Magnetic-potential-vector-and-gradient-tensorhttps://academic.oup.com/gji/article/239/2/821/7737672)
 759 [article/201/3/1977/782891/Magnetic-potential-vector-and-gradient](http://academic.oup.com/gji/article/201/3/1977/782891/Magnetic-potential-vector-and-gradient-tensorhttps://academic.oup.com/gji/article/239/2/821/7737672)
 760 [-tensorhttps://academic.oup.com/gji/article/239/2/821/7737672](https://academic.oup.com/gji/article/239/2/821/7737672) doi:
 761 10.1093/gji/ggae289
- 762 Bondár, I., & Storchak, D. (2011). Improved location procedures at the Interna-
 763 tional Seismological Centre. *Geophysical Journal International*, *186*(3), 1220–
 764 1244. Retrieved from www.isc.ac.uk doi: 10.1111/j.1365-246X.2011.05107.x
- 765 Brudzinski, M., Thurber, C., Hacker, B., & Engdahl, E. (2007). Global prevalence
 766 of double benioff zones. *Science*, *316*(5830), 1472–1474. doi: 10.1126/science
 767 .1139204
- 768 Craig, T. (2019, 2). Accurate Depth Determination for Moderate-Magnitude
 769 Earthquakes Using Global Teleseismic Data. *Journal of Geophysical*
 770 *Research: Solid Earth*, *124*(2), 1759–1780. Retrieved from [https://](https://onlinelibrary.wiley.com/doi/full/10.1029/2018JB016902https://onlinelibrary.wiley.com/doi/abs/10.1029/2018JB016902https://agupubs.onlinelibrary.wiley.com/doi/10.1029/2018JB016902)
 771 [onlinelibrary.wiley.com/doi/full/10.1029/2018JB016902https://](https://onlinelibrary.wiley.com/doi/full/10.1029/2018JB016902https://onlinelibrary.wiley.com/doi/abs/10.1029/2018JB016902https://agupubs.onlinelibrary.wiley.com/doi/10.1029/2018JB016902)
 772 [onlinelibrary.wiley.com/doi/abs/10.1029/2018JB016902https://](https://onlinelibrary.wiley.com/doi/abs/10.1029/2018JB016902https://agupubs.onlinelibrary.wiley.com/doi/10.1029/2018JB016902)
 773 agupubs.onlinelibrary.wiley.com/doi/10.1029/2018JB016902 doi:
 774 10.1029/2018JB016902
- 775 Craig, T., Methley, P., & Sandiford, D. (2022). Imbalanced moment release within
 776 subducting plates during initial bending and unbending. *Journal of Geophysi-*
 777 *cal Research: Solid Earth*, *127*(3), e2021JB023658.

- 778 Crotwell, H., Owens, T., & Ritsema, J. (1999). The TauP Toolkit: Flexible seismic
779 travel-time and ray-path utilities. *Seismological Research Letters*, *70*, 154–160.
- 780 Delouis, B., & Legrand, D. (2007). Mw 7.8 Tarapaca intermediate depth earthquake
781 of 13 June 2005 (northern Chile): Fault plane identification and slip distribu-
782 tion by waveform inversion. *Geophysical Research Letters*, *34*(1), 1–6. doi:
783 10.1029/2006GL028193
- 784 Dziewonski, A., Chou, T., & Woodhouse, J. (1981). Determination of earth-
785 quake source parameters from waveform data for studies of global and re-
786 gional seismicity. *Journal of Geophysical Research*, *86*(B4), 2825–2852. doi:
787 10.1029/JB086iB04p02825
- 788 Ekström, G., Nettles, M., & Dziewoński, A. (2012, 6). The global CMT project
789 2004-2010: Centroid-moment tensors for 13,017 earthquakes. *Physics of*
790 *the Earth and Planetary Interiors*, *200-201*, 1–9. Retrieved from [http://](http://dx.doi.org/10.1016/j.pepi.2012.04.002)
791 dx.doi.org/10.1016/j.pepi.2012.04.002 doi: 10.1016/j.pepi.2012.04.002
- 792 Engdahl, E., van der Hilst, R., & Buland, R. (1998). Global teleseismic earthquake
793 relocation with improved travel times and procedures for depth determina-
794 tion. *Bulletin of the Seismological Society of America*, *88*(3), 722–743. doi:
795 10.1785/bssa0880030722
- 796 Espurt, N., Funicello, F., Martinod, J., Guillaume, B., Regard, V., Faccenna, C., &
797 Brusset, S. (2008). Flat subduction dynamics and deformation of the South
798 American plate: Insights from analog modeling. *Tectonics*, *27*(3), 1–19. doi:
799 10.1029/2007TC002175
- 800 Ester, M., Kriegel, H., Sander, J., & Xu, X. (1996). A Density-Based Algorithm
801 for Discovering Clusters A Density-Based Algorithm for Discovering Clusters
802 in Large Spatial Databases with Noise. In *Proceedings - 2nd international*
803 *conference on knowledge discovery and data mining, kdd 1996* (pp. 226–231).
804 Retrieved from www.aaai.org
- 805 Flament, N., Gurnis, M., Müller, R., Bower, D., & Husson, L. (2015). Influence of
806 subduction history on South American topography. *Earth and Planetary Sci-*
807 *ence Letters*, *430*, 9–18. Retrieved from [http://dx.doi.org/10.1016/j.epsl](http://dx.doi.org/10.1016/j.epsl.2015.08.006)
808 [.2015.08.006](http://dx.doi.org/10.1016/j.epsl.2015.08.006) doi: 10.1016/j.epsl.2015.08.006
- 809 Florez, M., & Prieto, G. (2017, 6). Precise relative earthquake depth de-
810 termination using array processing techniques. *Journal of Geophysical*
811 *Research: Solid Earth*, *122*(6), 4559–4571. Retrieved from [https://](https://onlinelibrary.wiley.com/doi/full/10.1002/2017JB014132)
812 onlinelibrary.wiley.com/doi/full/10.1002/2017JB014132[https://](https://onlinelibrary.wiley.com/doi/abs/10.1002/2017JB014132)
813 onlinelibrary.wiley.com/doi/abs/10.1002/2017JB014132[https://](https://agupubs.onlinelibrary.wiley.com/doi/10.1002/2017JB014132)
814 agupubs.onlinelibrary.wiley.com/doi/10.1002/2017JB014132 doi:
815 10.1002/2017JB014132
- 816 Florez, M., & Prieto, G. (2019, 4). Controlling Factors of Seismicity and Geometry
817 in Double Seismic Zones. *Geophysical Research Letters*, *46*(8), 4174–4181. doi:
818 10.1029/2018GL081168
- 819 Gao, Y., Yuan, X., Heit, B., Tilmann, F., van Herwaarden, D., Thrastarson, S.,
820 ... Schurr, B. (2021, 11). Impact of the Juan Fernandez Ridge on the Pam-
821 pean Flat Subduction Inferred From Full Waveform Inversion. *Geophys-*
822 *ical Research Letters*, *48*(21), e2021GL095509. Retrieved from [https://](https://onlinelibrary.wiley.com/doi/full/10.1029/2021GL095509)
823 onlinelibrary.wiley.com/doi/full/10.1029/2021GL095509[https://](https://onlinelibrary.wiley.com/doi/abs/10.1029/2021GL095509)
824 onlinelibrary.wiley.com/doi/abs/10.1029/2021GL095509[https://](https://agupubs.onlinelibrary.wiley.com/doi/10.1029/2021GL095509)
825 agupubs.onlinelibrary.wiley.com/doi/10.1029/2021GL095509 doi:
826 10.1029/2021GL095509
- 827 Global Volcanism Program, S. I. (2024). *Volcanoes of the World, v. 5.2.7*. Re-
828 trieved from <https://volcano.si.edu/> doi: [https://doi.org/10.5479/si.GVP](https://doi.org/10.5479/si.GVP.VOTW5-2024.5.2)
829 [.VOTW5-2024.5.2](https://doi.org/10.5479/si.GVP.VOTW5-2024.5.2)
- 830 Hayes, G. (2017). The finite, kinematic rupture properties of great-sized earthquakes
831 since 1990. *Earth and Planetary Science Letters*, *468*, 94–100. Retrieved from
832 www.elsevier.com/locate/epsl doi: 10.1016/j.epsl.2017.04.003

- 833 Hayes, G., Moore, G., Portner, D., Hearne, M., Flamme, H., Furtney, M., &
834 Smoczyk, G. (2018, 10). Slab2, a comprehensive subduction zone geome-
835 try model. *Science*, *362*(6410), 58–61. doi: 10.1126/science.aat4723
- 836 Hayes, G., Wald, D., & Johnson, R. (2012). Slab1.0: A three-dimensional model
837 of global subduction zone geometries. *Journal of Geophysical Research: Solid*
838 *Earth*, *117*(1), 1–15. doi: 10.1029/2011JB008524
- 839 Hosseini, K., & Sigloch, K. (2017). ObspyDMT: A Python toolbox for retrieving and
840 processing large seismological data sets. *Solid Earth*, *8*(5), 1047–1070. doi: 10
841 .5194/se-8-1047-2017
- 842 Hu, Y., Yagi, Y., Okuwaki, R., & Shimizu, K. (2021). Back-propagating rupture
843 evolution within a curved slab during the 2019 Mw8.0 Peru intraslab earth-
844 quake. *Geophysical Journal International*, *227*(3), 1602–1611. Retrieved from
845 <https://doi.org/10.1093/gji/ggab303> doi: 10.1093/gji/ggab303
- 846 International Seismological Centre. (2024). *On-line Bulletin*. [https://doi.org/10](https://doi.org/10.31905/D808B830)
847 [.31905/D808B830](https://doi.org/10.31905/D808B830).
- 848 Kennett, B., Engdahl, E., & Buland, R. (1995). Constraints on seismic velocities
849 in the Earth from traveltimes. *Geophysical Journal International*, *122*(1), 108–
850 124. doi: 10.1111/j.1365-246X.1995.tb03540.x
- 851 Kuge, K., Kase, Y., Urata, Y., Campos, J., & Perez, A. (2010). Rupture charac-
852 teristics of the 2005 Tarapaca, northern Chile, intermediate-depth earthquake:
853 Evidence for heterogeneous fluid distribution across the subducting oceanic
854 plate? *Journal of Geophysical Research: Solid Earth*, *115*(9), 1–15. doi:
855 10.1029/2009JB007106
- 856 Liu, W., & Yao, H. (2020, 2). Rupture Process of the 26 May 2019 Mw 8.0 Northern
857 Peru Intermediate-Depth Earthquake and Insights Into Its Mechanism. *Geo-*
858 *physical Research Letters*, *47*(4). doi: 10.1029/2020GL087167
- 859 Luo, H., Zeng, H., Shi, Q., Wang, T., Liao, M., Hu, J., & Wei, S. (2023). Could
860 thermal pressurization have induced the frequency-dependent rupture during
861 the 2019 m w8. 0 peru intermediate-depth earthquake? *Geophysical Journal*
862 *International*, *232*(1), 115–127.
- 863 Münchmeyer, J., Saul, J., & Tilmann, F. (2024). Learning the Deep and
864 the Shallow: Deep-Learning-Based Depth Phase Picking and Earthquake
865 Depth Estimation. *Seismological Research Letters*, *95*(3), 1543–1557. doi:
866 10.1785/0220230187
- 867 Pedregosa, F., Michel, V., Grisel, O., Blondel, M., Prettenhofer, P., Weiss, R.,
868 ... Duchesnay, E. (2011). Scikit-learn: Machine Learning in Python
869 Gaël Varoquaux Bertrand Thirion Vincent Dubourg Alexandre Passos
870 PEDREGOSA, VAROQUAUX, GRAMFORT ET AL. Matthieu Perrot.
871 *Journal of Machine Learning Research*, *12*, 2825–2830. Retrieved from
872 <http://scikit-learn.sourceforge.net>.
- 873 Peyrat, S., Campos, J., de Chabalier, J., Perez, A., Bonvalot, S., Bouin, M. P., ...
874 Vilotte, J. (2006). Tarapacá intermediate-depth earthquake (Mw 7.7, 2005,
875 northern Chile): A slab-pull event with horizontal fault plane constrained from
876 seismologic and geodetic observations. *Geophysical Research Letters*, *33*(22),
877 1–6. doi: 10.1029/2006GL027710
- 878 Portner, D., & Hayes, G. (2018). Incorporating teleseismic tomography data
879 into models of upper mantle slab geometry. *Geophysical Journal Interna-*
880 *tional*, *215*(1), 325–332. Retrieved from [https://academic.oup.com/gji/](https://academic.oup.com/gji/article-abstract/215/1/325/5053066)
881 [article-abstract/215/1/325/5053066](https://academic.oup.com/gji/article-abstract/215/1/325/5053066) doi: 10.1093/gji/ggy279
- 882 Rodríguez, E., Beck, S., Ruiz, M., Meltzer, A., Portner, D., Hernández, S., ...
883 Charvis, P. (2024). Seismic imaging of the Northern Andean subduction zone
884 from teleseismic tomography: a torn and fragmented Nazca slab. *Geophysical*
885 *Journal International*, *236*(1), 593–606. doi: 10.1093/gji/ggad421
- 886 Sandiford, D., Moresi, L., Sandiford, M., Farrington, R., & Yang, T. (2020, 8). The
887 Fingerprints of Flexure in Slab Seismicity. *Tectonics*, *39*(8). doi: 10.1029/

- 943 Zandt, G., Velasco, A., & Beck, S. (1994). Composition and thickness of the south-
944 ern Altiplano crust, Bolivia. *Geology*, *22*(11), 1003–1006. doi: 10.1130/0091-
945 -7613(1994)022(1003:CATOTS)2.3.CO;2
- 946 Zeng, L., Ye, L., Yao, H., Liu, W., Si, D., Lay, T., & Yang, T. (2025). Narrow
947 intermediate-depth seismogenic band related to flexural strain in relatively
948 dry Peruvian flat slab. *Communications Earth and Environment*, *6*(1), 1–14.
949 Retrieved from <http://dx.doi.org/10.1038/s43247-025-02071-0> doi:
950 10.1038/s43247-025-02071-0

Supplementary Material

Assessing the impact of automatically derived depth phases on the determination of earthquake hypocentres – application to the South America subduction zone

Alice Blackwell¹, Timothy Craig², Sebastian Rost¹, Thomas Garth³, and Ryan Gallacher³

¹Institute for Geophysics and Tectonics, University of Leeds, Leeds, UK

²COMET, Institute for Geophysics and Tectonics, University of Leeds, Leeds, UK

³International Seismological Centre, Pipers Lane, Thatcham, Berkshire, RG19 4NS, UK

Corresponding author: Alice Blackwell (ee18ab@leeds.ac.uk)

Date: June 19, 2025

1 Figures

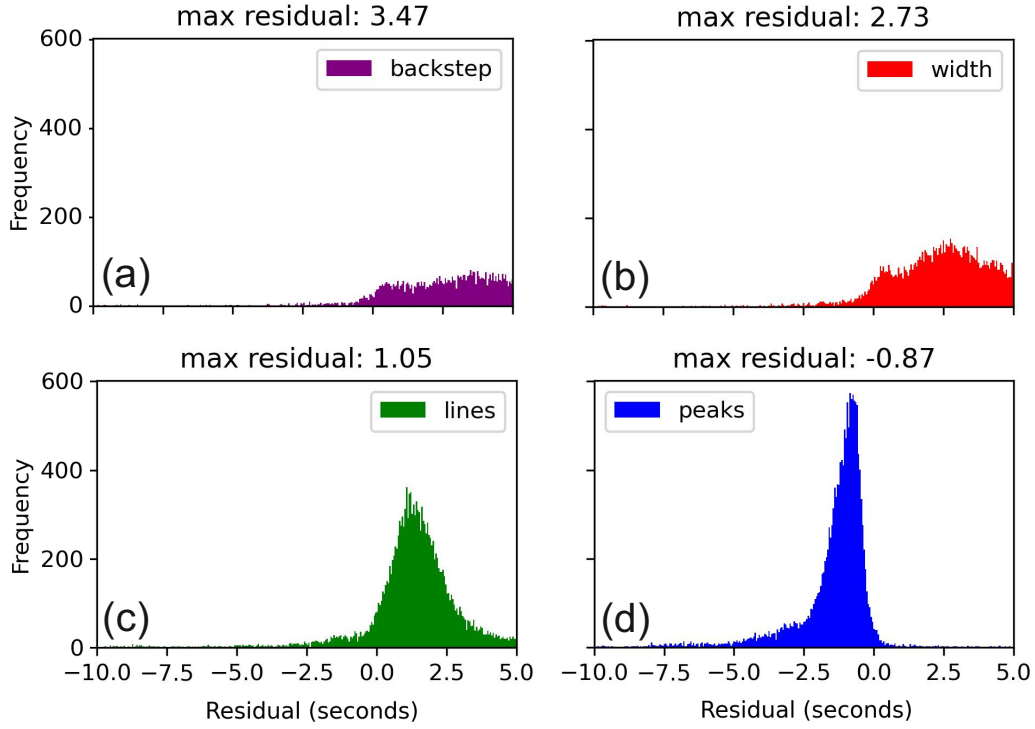


Figure S1. Plot of the residual between the slowness corrected, median ISC reported direct *P* arrival for an *ad-hoc* array and (a) the onset approximation using back-stepping from the peak to below a noise threshold, (b) the onset approximation using the intersection of the envelope with a horizontal line projected at 0.9 of the *P* peak height, (c) the onset approximation using two lines, and (d) the *ad-hoc* array determined peak amplitude pick. The plots demonstrate the inconsistency in using a geometric phase onset determination, and show that these are typically 1-3.5 seconds early compared to the slowness corrected, median ISC reported direct *P* arrival. (d) also shows that the mode difference between the amplitude pick and the ISC onset pick is 0.87 seconds for the data. These are calculated for the Peruvian and northern Chilean catalogues presented in Blackwell et al. (2024), and the histograms are calculated at a 0.01 resolution.

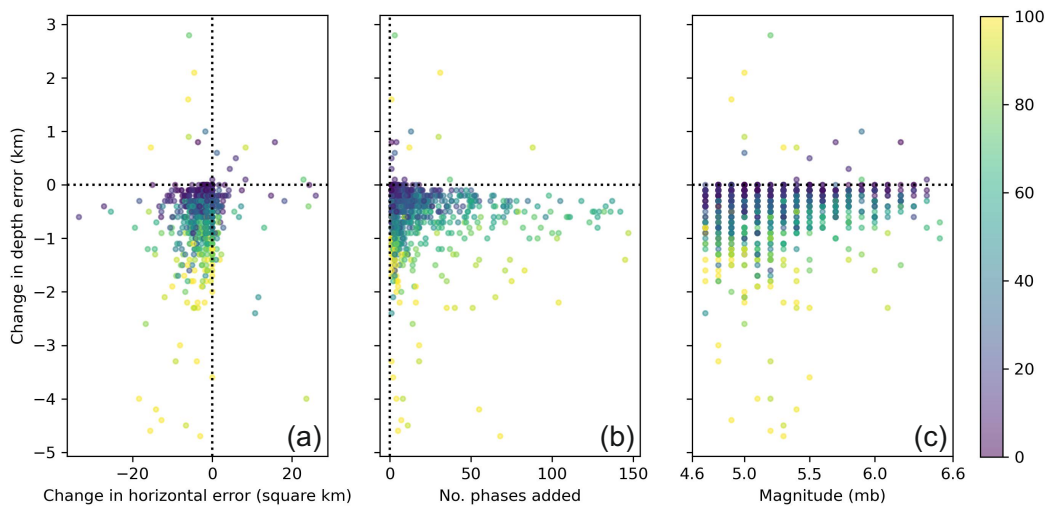


Figure S2. Change in depth error between the reported and augmented ISC catalogue results versus horizontal error ellipse reduction (a), the number of time-defining phases added by the *ad-hoc* arrays in the augmented ISC results (b), and magnitude (c). Scatter points are coloured by the percentage increase in time-defining depth phases. Events which did not have new time-defining phases from the augmented ISC input are not plotted.

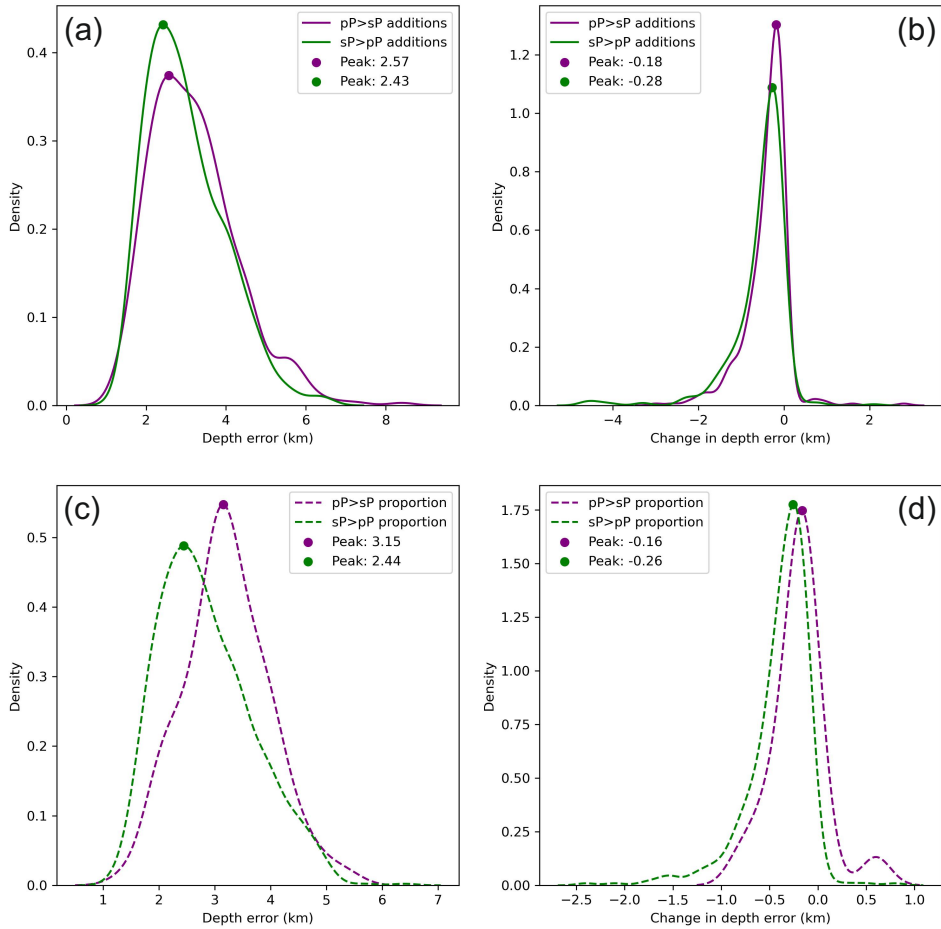


Figure S3. Probability density functions for the depth errors in the augmented ISC catalogue results, and change in depth error when compared to the reported ISC results. When *ad-hoc* arrays add more time-defining *pP* than *sP* phases to an event, or vice versa (a and b), and when *ad-hoc* arrays add a larger proportion of *pP* (relative to the number of time-defining *pP* phases) than *sP* (relative to the number of time-defining *sP* phases) phases to the event catalogue, and vice versa (c and d). Events which did not have new time-defining phases from the augmented ISC input are not plotted.

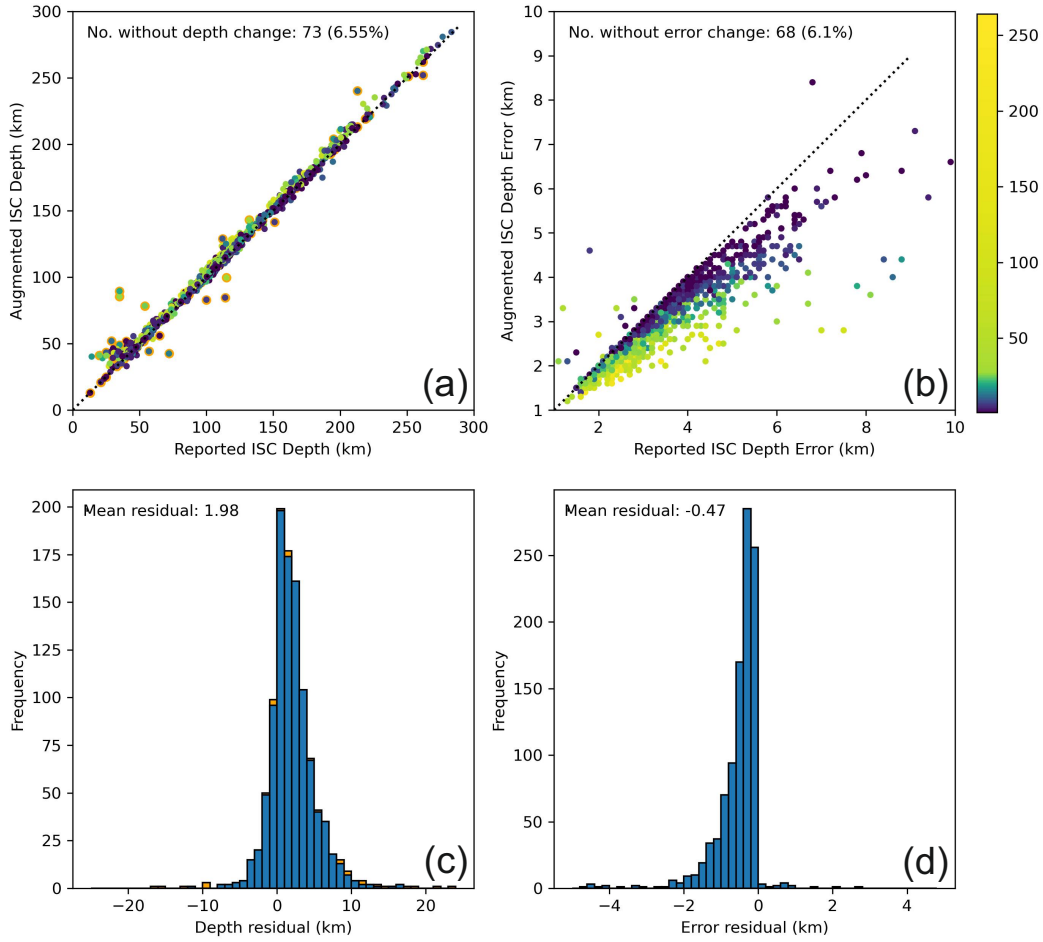


Figure S4. Comparison of depth and depth error between the reported ISC and the augmented ISC inputs without *S* coda picks when applying ISCloc. (a) and (b) show the depth and depth error change when additional *ad-hoc* array phases are included. Both plots are coloured by number of additional time-defining phases, and (a) also has orange outlines for events which had fixed depths prior to the addition of phases. (c) and (d) are histograms showing the residual between the reported ISC and augmented ISC depths and depth errors respectively. (c) has orange bars indicating residual in depth when the fixed events are included. Events which did not have new time-defining phases from the augmented ISC input are not plotted.

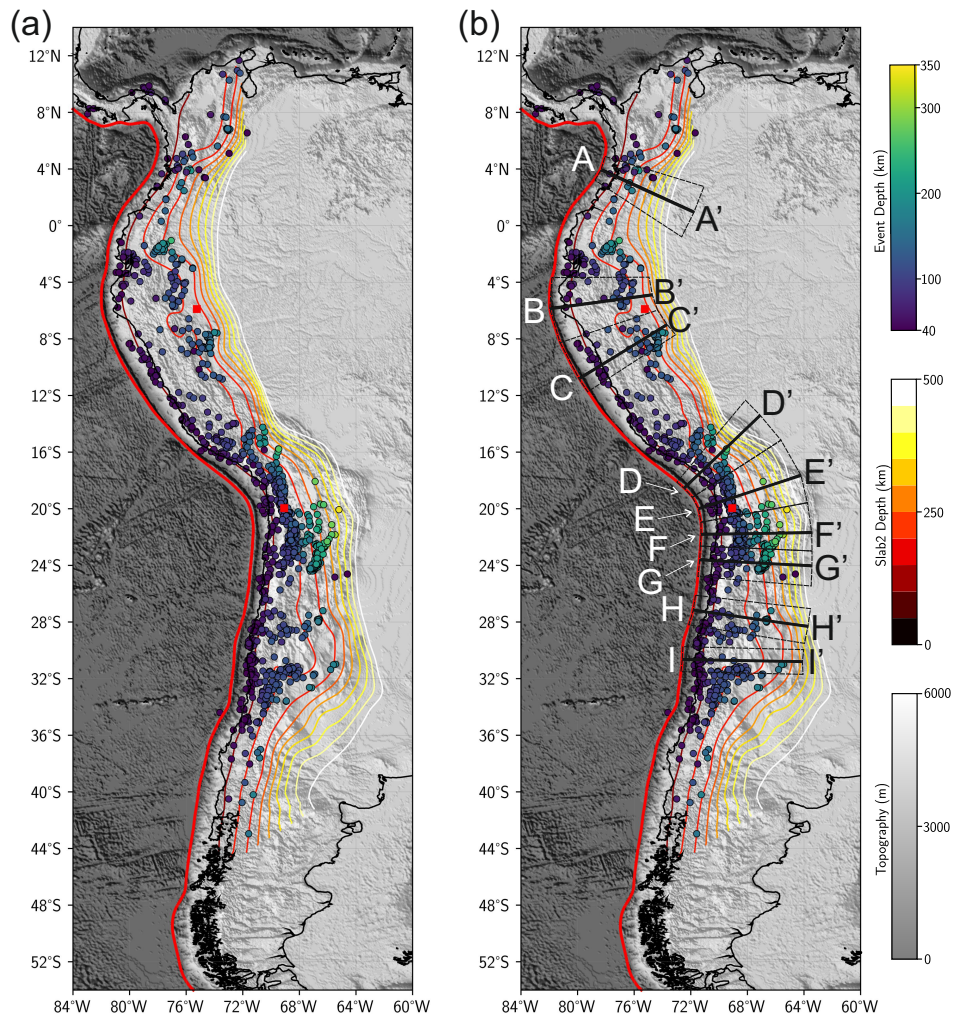


Figure S5.

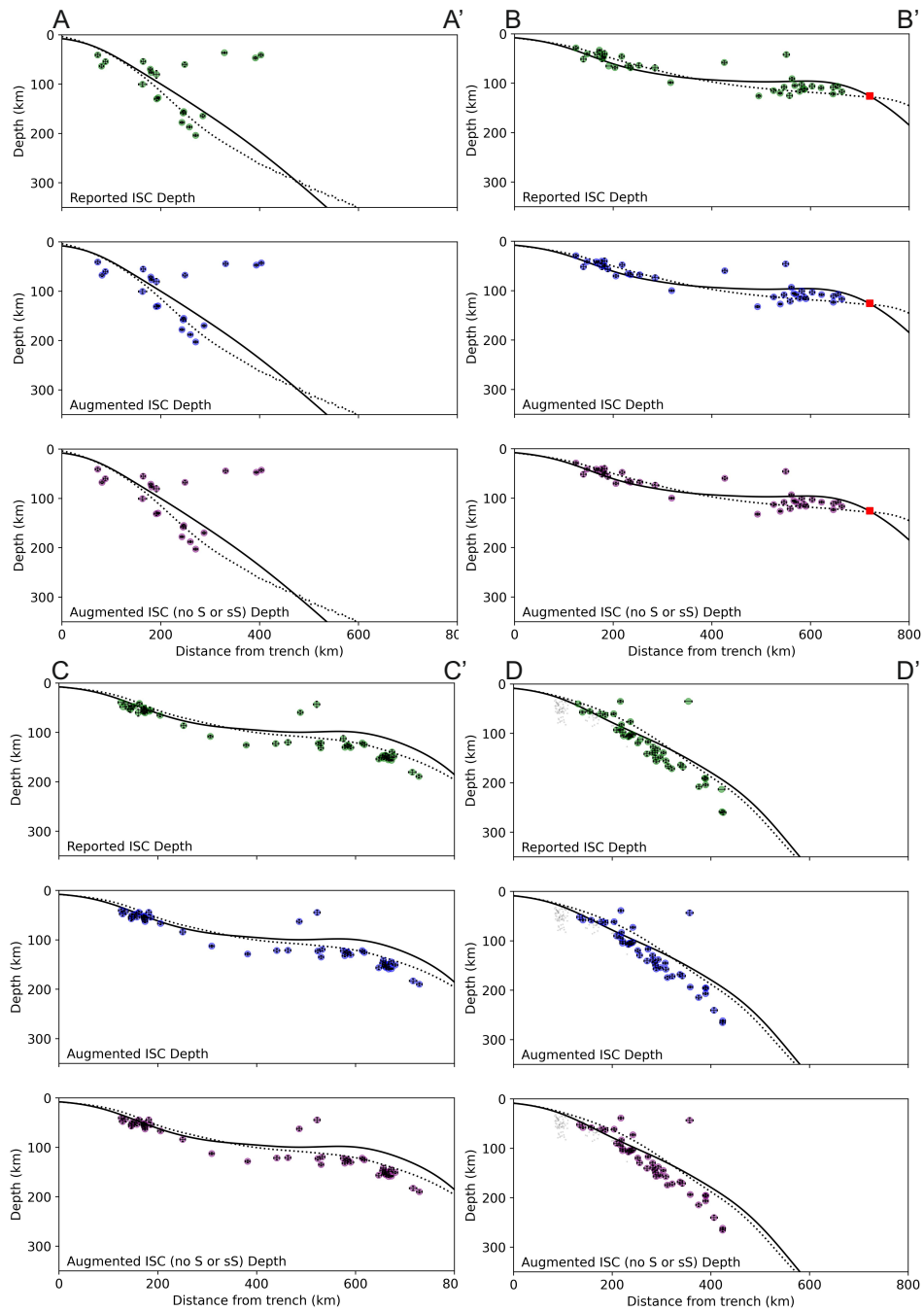


Figure S6.

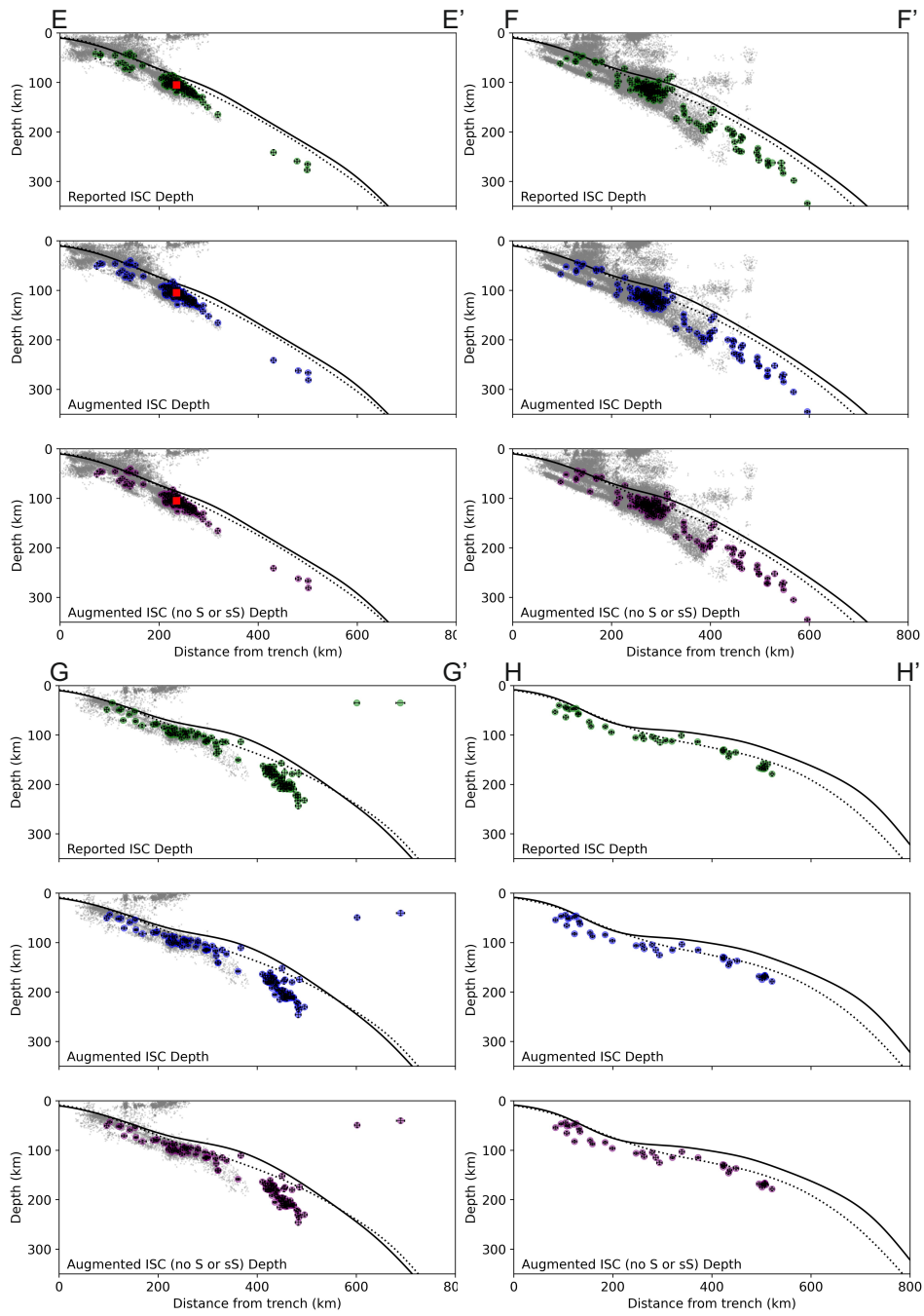


Figure S7.

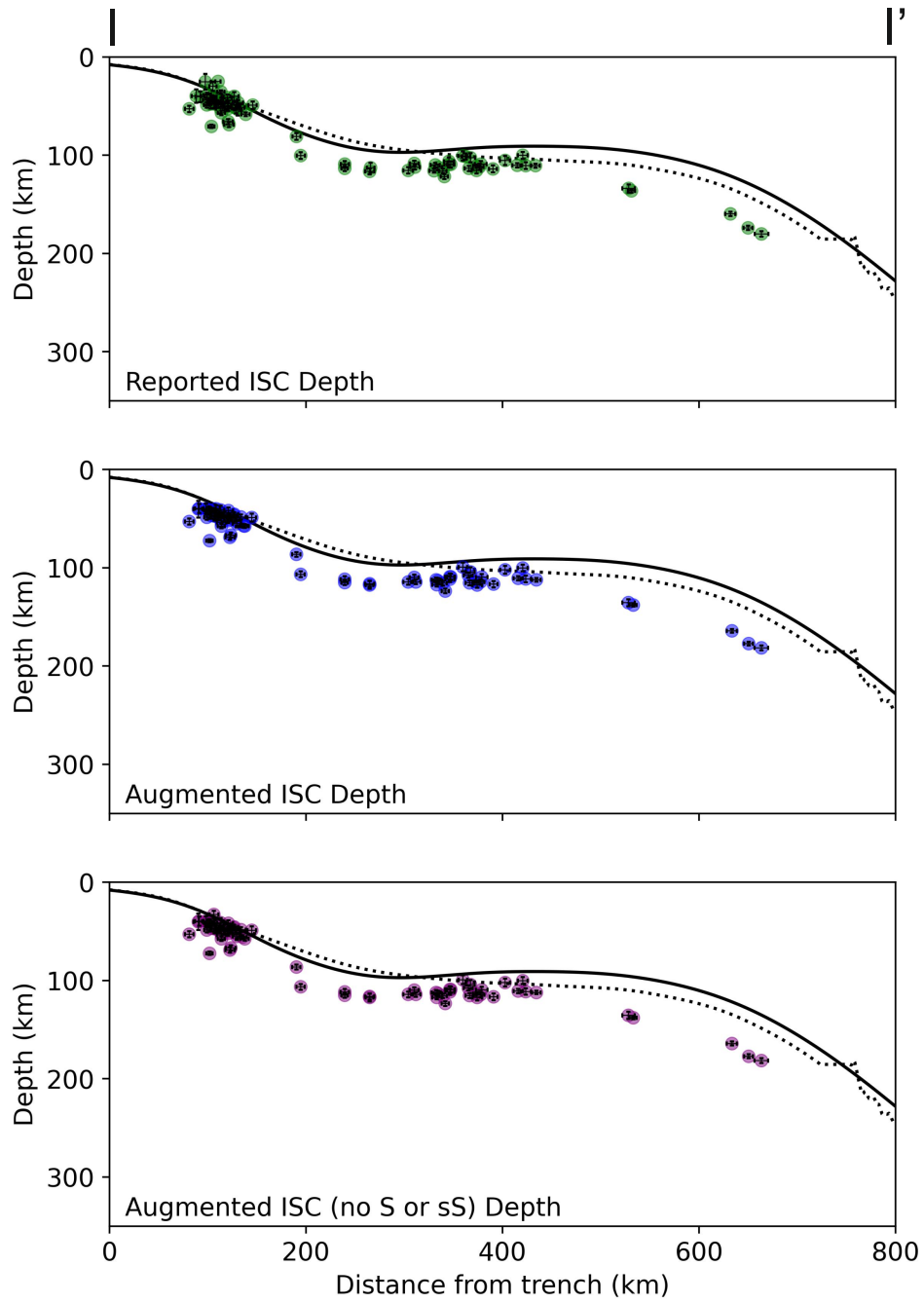


Figure S8.

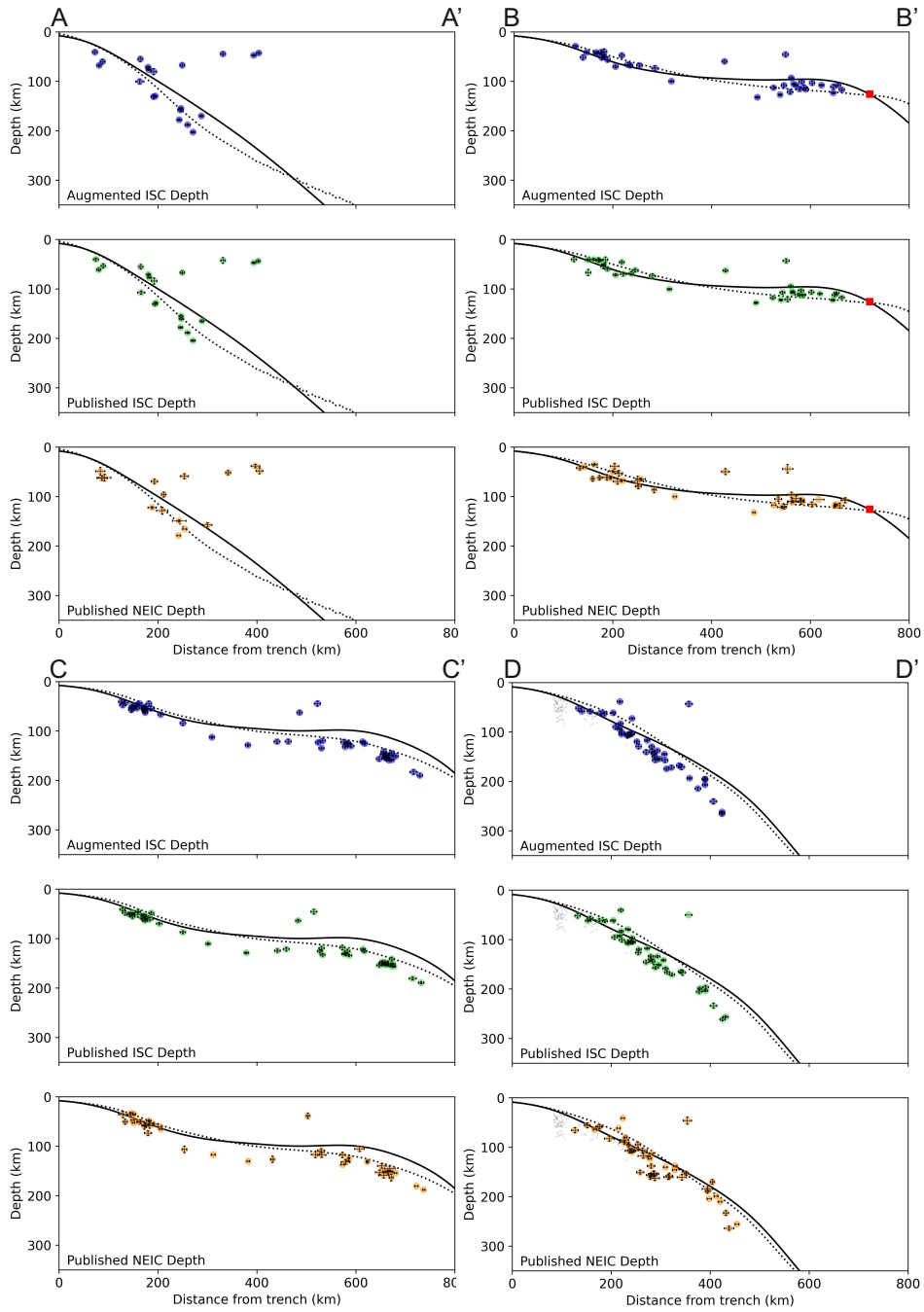


Figure S9.

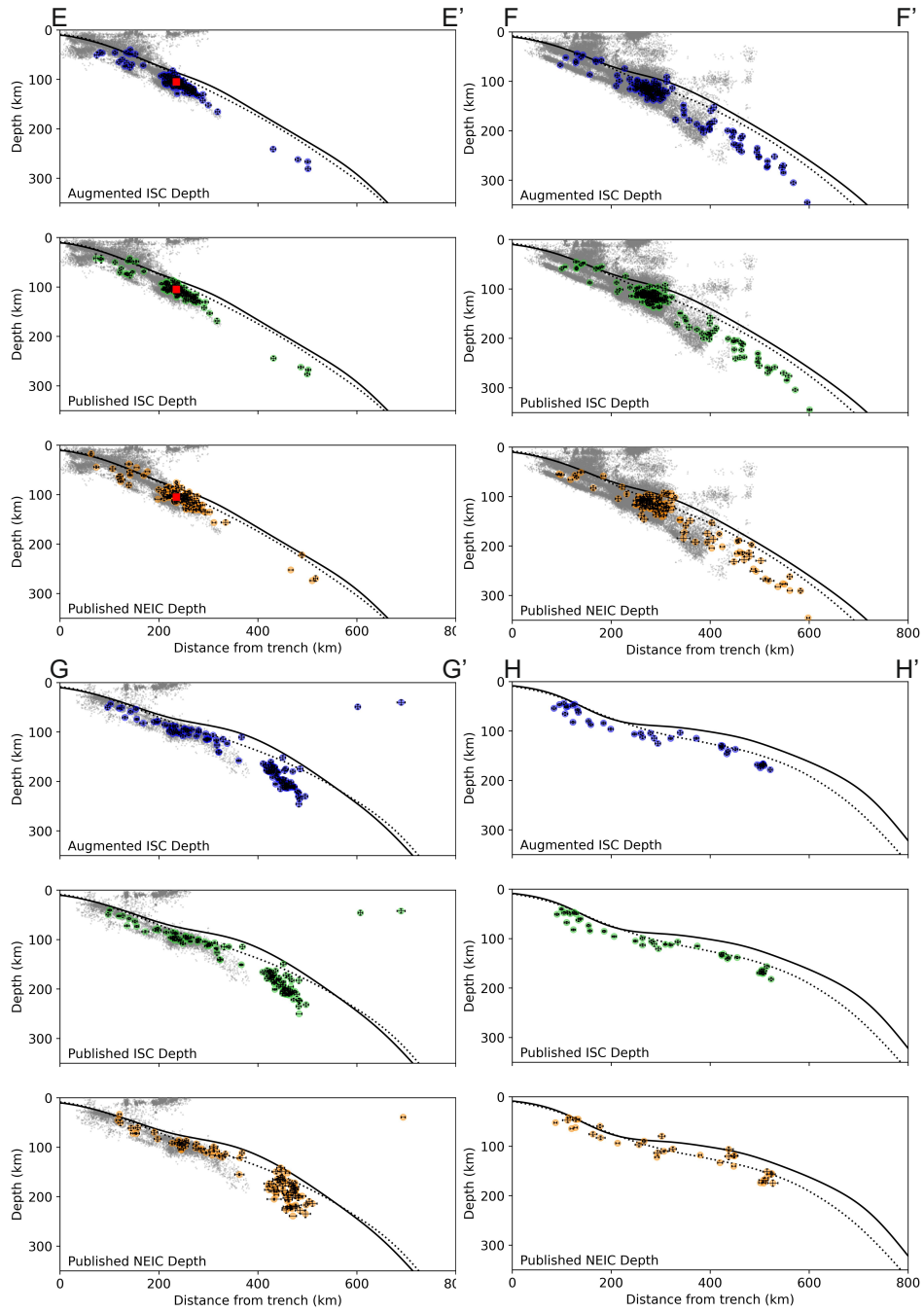


Figure S10.

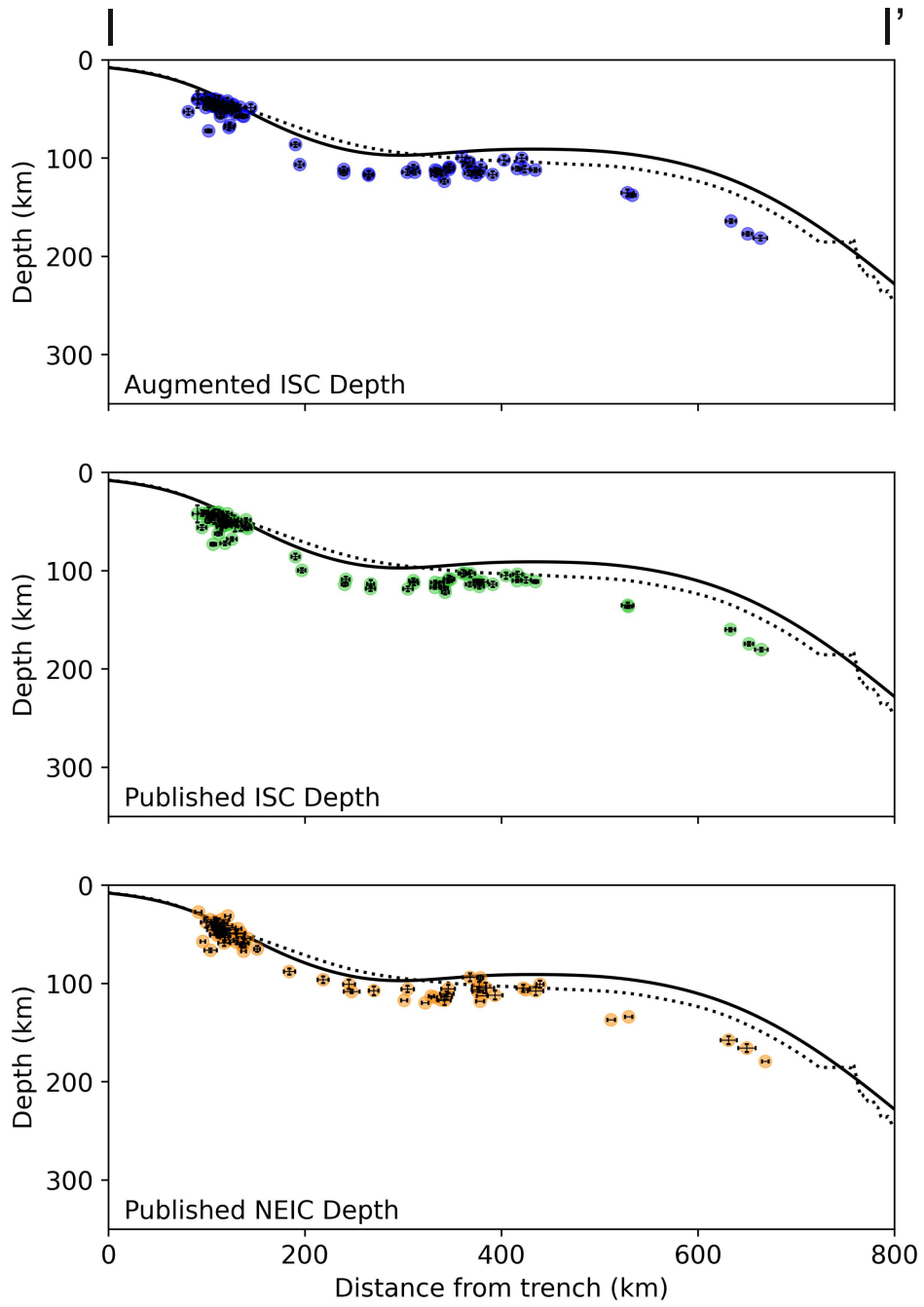


Figure S11.

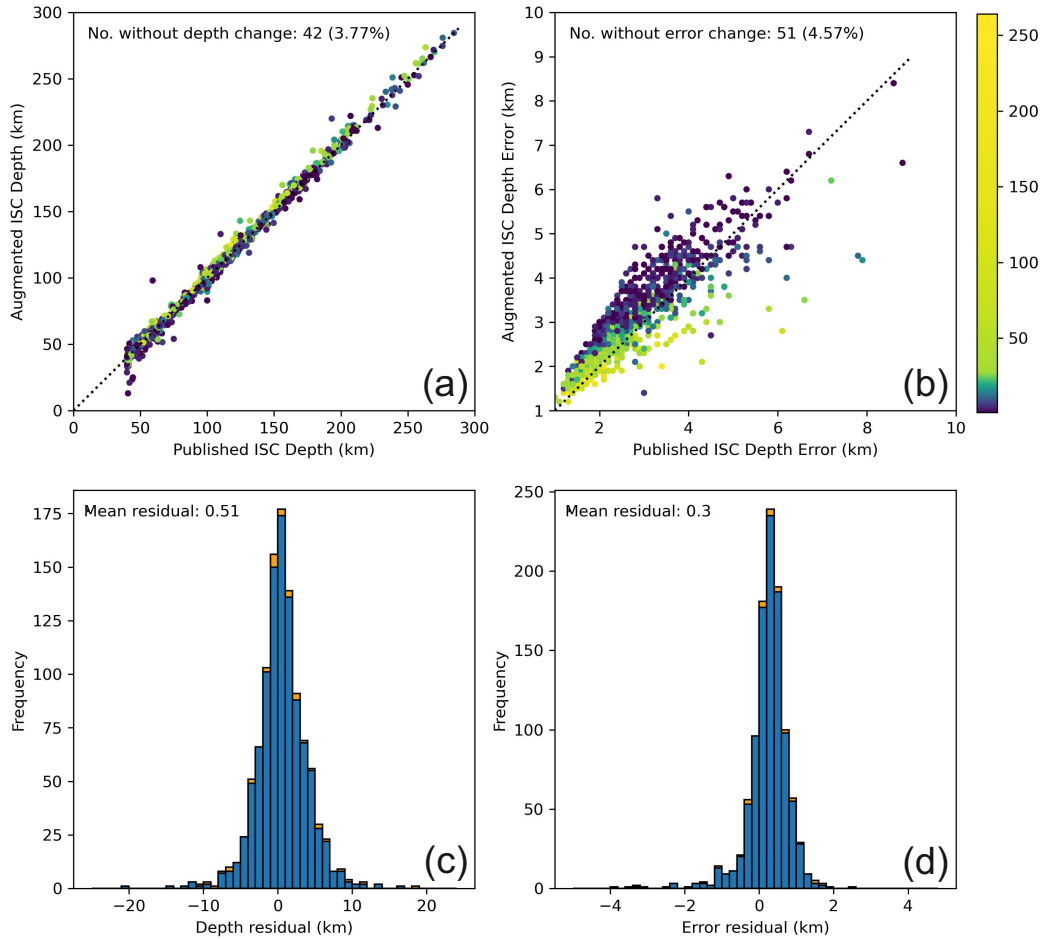


Figure S12. Comparison of depth and depth error between the published ISC and augmented ISC inputs when applying ISCloc. (a) and (b) show the depth and depth error change when additional *ad-hoc* array phases are included. Both plots are coloured by number of additional time-defining phases, and (a) also has orange outlines for events which had fixed depths prior to the addition of phases. (c) and (d) are histograms showing the residual between the reported ISC and augmented ISC depths and depth errors respectively. (c) has orange bars indicating residual in depth when the fixed events are included. Events which did not have new time-defining phases from the augmented ISC input are not plotted.

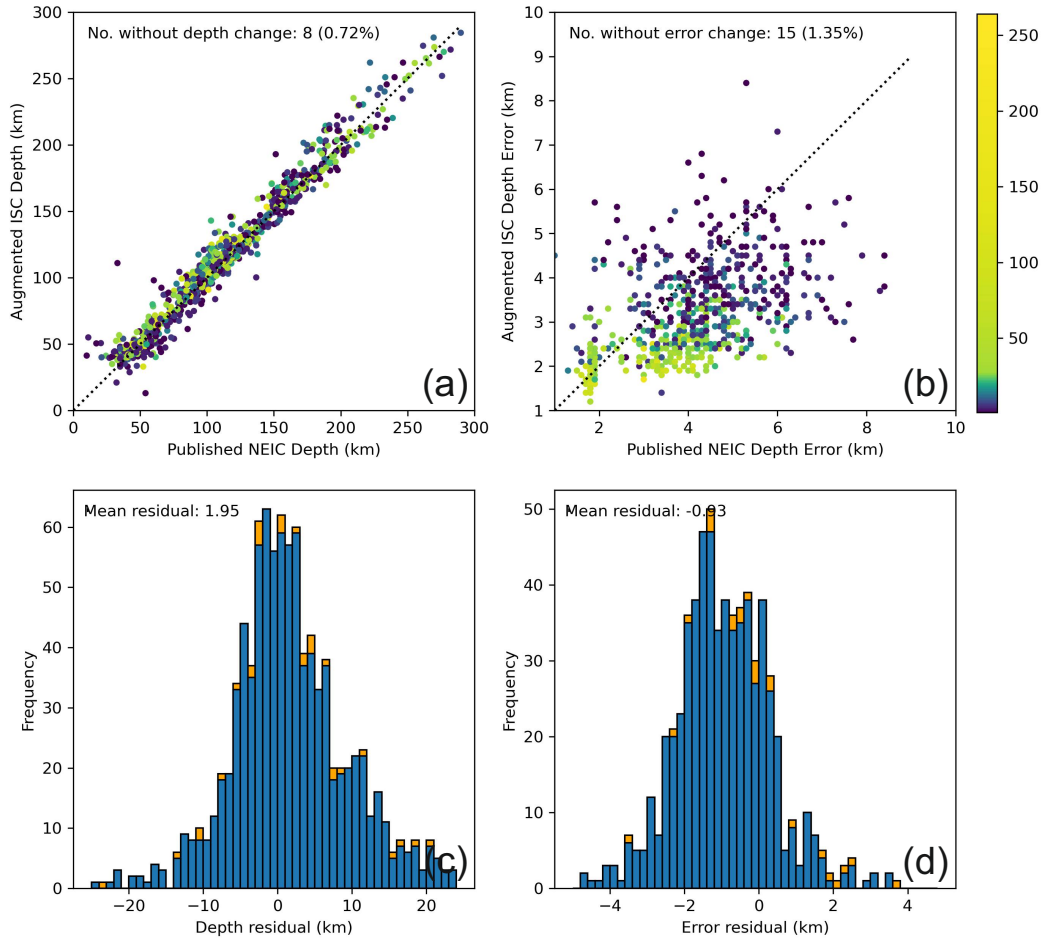


Figure S13. Comparison of depth and depth error between the published NEIC and augmented ISC inputs when applying ISCloc. (a) and (b) show the depth and depth error change when additional *ad-hoc* array phases are included. Both plots are coloured by number of additional time-defining phases, and (a) also has orange outlines for events which had fixed depths prior to the addition of phases. (c) and (d) are histograms showing the residual between the reported ISC and augmented ISC depths and depth errors respectively. (c) has orange bars indicating residual in depth when the fixed events are included. Events which did not have new time-defining phases from the augmented ISC input are not plotted.

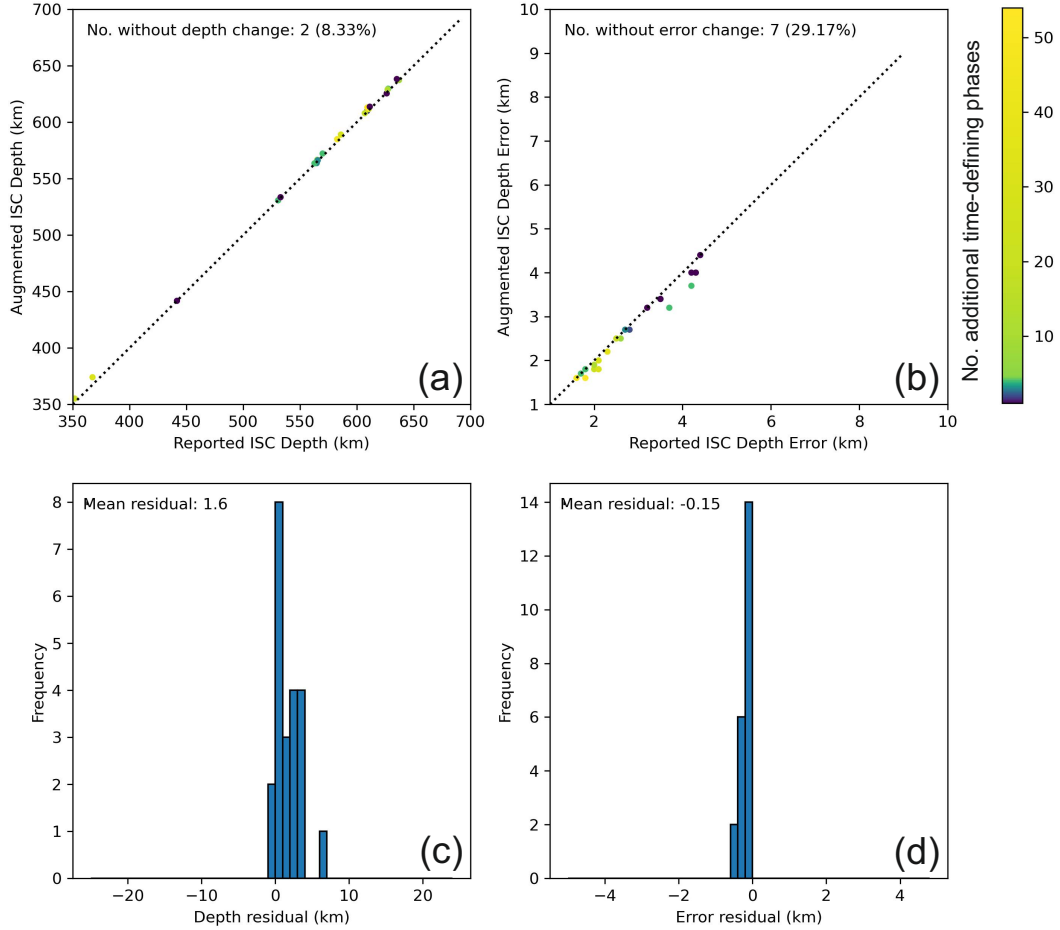


Figure S14. Comparison of depth and depth error between the reported ISC and augmented ISC inputs when applying ISClocc to deep focus events. (a) and (b) show the depth and depth error change when additional *ad-hoc* array phases are included. Both plots are coloured by number of additional time-defining phases, and (a) also has orange outlines for events which had fixed depths prior to the addition of phases. (c) and (d) are histograms showing the residual between the reported ISC and augmented ISC depths and depth errors respectively. (c) has orange bars indicating residual in depth when the fixed events are included. Events which did not have new time-defining phases from the augmented ISC input are not plotted.